The Astronomical Journal, 139:228–251, 2010 January doi:10.1088/0004-6256/139/1/228

THE ARCHITECTURE OF THE CASSINI DIVISION

M. M. Hedman[1], P. D. Nicholson[1], K. H. Baines[2], B. J. Buratti[2], C. Sotin[2], R. N. Clark[3], R. H. Brown[4], R. G. French[5], and E. A. Marouf[6]

[1] Department of Astronomy, Cornell University, Ithaca, NY 14853, USA; mmhedman@astro.cornell.edu
[2] Jet Propulsion Lab, Pasadena, CA 91109, USA
[3] United States Geological Survey, Denver, CO 80225, USA
[4] Lunar and Planetary Lab, University of Arizona, Tucson, AZ 85721, USA
[5] Department of Astronomy, Wellesley College, Wellesley, MA 02481, USA
[6] Department of Electrical Engineering, San Jose State University, San Jose, CA 95192, USA
Received 2009 July 17; accepted 2009 November 5; published 2009 December 10

ABSTRACT

The Cassini Division in Saturn's rings contains a series of eight named gaps, three of which contain dense ringlets. Observations of stellar occultations by the Visual and Infrared Mapping Spectrometer onboard the Cassini spacecraft have yielded ∼40 accurate and precise measurements of the radial position of the edges of all of these gaps and ringlets. These data reveal suggestive patterns in the shapes of many of the gap edges: the outer edges of the five gaps without ringlets are circular to within 1 km, while the inner edges of six of the gaps are eccentric, with apsidal precession rates consistent with those expected for eccentric orbits near each edge. Intriguingly, the pattern speeds of these eccentric inner gap edges, together with that of the eccentric Huygens Ringlet, form a series with a characteristic spacing of 0.°06 day^{-1}. The two gaps with non-eccentric inner edges lie near first-order inner Lindblad resonances (ILRs) with moons. One such edge is close to the 5:4 ILR with Prometheus, and the radial excursions of this edge do appear to have an $m = 5$ component aligned with that moon. The other resonantly confined edge is the outer edge of the B ring, which lies near the 2:1 Mimas ILR. Detailed investigation of the B-ring-edge data confirm the presence of an $m = 2$ perturbation on the B-ring edge, but also show that during the course of the Cassini Mission, this pattern has drifted backward relative to Mimas. Comparisons with earlier occultation measurements going back to *Voyager* suggest the possibility that the $m = 2$ pattern is actually librating relative to Mimas with a libration frequency $L \sim 0.°06$ day^{-1} (or possibly 0.°12 day^{-1}). In addition to the $m = 2$ pattern, the B-ring edge also has an $m = 1$ component that rotates around the planet at a rate close to the expected apsidal precession rate ($\dot{\varpi}_B \sim 5.°06$ day^{-1}). Thus, the pattern speeds of the eccentric edges in the Cassini Division can be generated from various combinations of the pattern speeds of structures observed on the edge of the B ring: $\Omega_p = \dot{\varpi}_B - jL$ for $j = 1, 2, 3, \ldots, 7$.We therefore suggest that most of the gaps in the Cassini Division are produced by resonances involving perturbations from the massive edge of the B ring. We find that a combination of gravitational perturbations generated by the radial excursions in the B-ring edge and the gravitational perturbations from the Mimas 2:1 ILR yields terms in the equations of motion that should act to constrain the pericenter location of particle orbits in the vicinity of each of the eccentric inner gap edges in the Cassini Division. This alignment of pericenters could be responsible for forming the Cassini-Division Gaps and thus explain why these gaps are located where they are.

Key words: occultations – planets: rings

Online-only material: color figures

1. INTRODUCTION

The Cassini Division is a roughly 4500 km wide region in Saturn's main rings situated between the A and B rings. Far from being a completely empty gap between these two rings, this zone is actually a complex region containing an array of gaps and ringlets. The physical processes responsible for creating and maintaining most of the observed features in this region remain obscure.

In particular, there is still no definitive explanation for most of the numerous gaps present throughout the inner part of Cassini Division. As shown in Figure 1, there are eight gaps in the inner part of the Cassini Division, all of which are now named after various researchers who worked on Saturn's rings (Colwell et al. 2009). The innermost gap is called the Huygens Gap and it marks the inner boundary of the Cassini Division. The inner edge of the Huygens Gap, which is also the outer edge of the massive B ring, has long been known to be associated with a 2:1 mean-motion resonance with Saturn's moon Mimas (Porco et al. 1984). This gap contains two optically thick ringlets: the inner one, called the "Huygens Ringlet," is known to be eccentric, while the outer, or "Strange" ringlet seems to have a significant inclination (Turtle et al. 1991; Spitale & Porco 2006; Spitale et al. 2008).

While the Mimas 2:1 resonance likely plays an important role in creating the Huygens Gap, the origins of the other seven gaps, as well as the dense ringlets in the Huygens, Herschel, and Laplace Gaps, are much less clear. Some have argued that each gap in the Cassini Division contains a tiny moon (Lissauer et al. 1981), just as the Encke and Keeler Gaps in the A ring are maintained by the small moons, Pan and Daphnis. While some wavelike features in the Cassini Division have been interpreted as evidence for the existence of such moons (Marouf & Tyler 1986), direct detections of the moons themselves have not yet been reported. It is also not clear why such moons would be concentrated in this particular part of the ring system, well inside Saturn's Roche limit for icy bodies.

Using the extensive occultation data obtained by the Visual and Infrared Mapping Spectrometer (VIMS) onboard the Cassini spacecraft, we have conducted an investigation of the

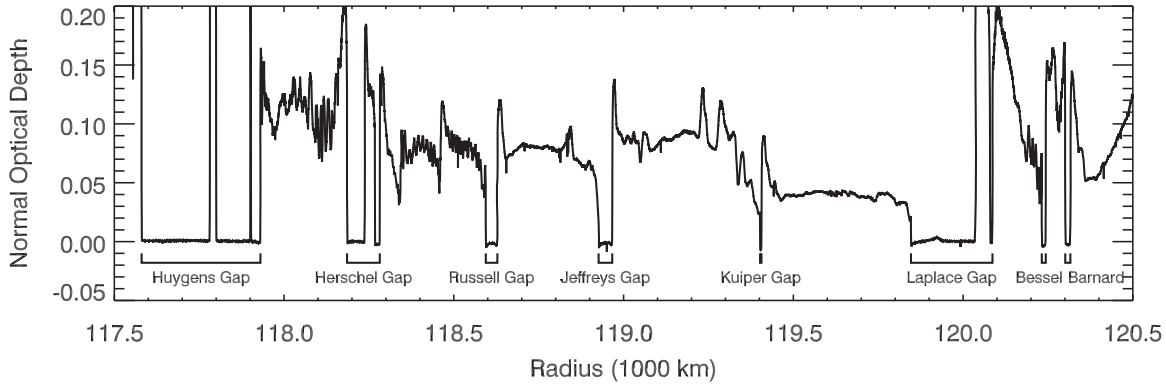

Figure 1. Overview of the basic architecture of the inner part of the Cassini Division. This optical depth profile is derived from the Rev 8 ingress occultation of *o* Ceti by the rings observed by the VIMS instrument on board Cassini. The various gaps discussed in this study are labeled.

gaps in the Cassini Division. The high-resolution and accurate geometrical information possible with these data has enabled us to determine the shapes of most of the edges of these gaps and ringlets. Based on this information, we will propose alternative explanations for these gaps that do not require the existence of a small moon within each and every gap.

Section 2 of this paper describes the VIMS observations used in this analysis, and how they were processed to obtain position estimates for the various edges. Section 3 presents the results of our analysis and the derived constraints on the shapes of various edges in the Cassini Division, including the B-ring edge. The B-ring edge turns out to be quite complex, so Section 4 briefly compares some of this edge's observed features to the predictions from simple dynamical models. Section 5 presents a dynamical model that could explain the location of the inner edges of the various gaps in the Cassini Division as the result of a series of resonances involving perturbations from the massive B-ring edge. This model is only a first step toward understanding the architecture of the Cassini Division, so Section 6 discusses potential future work that could confirm and extend this model. The final section summarizes our conclusions.

2. OBSERVATIONS AND DATA REDUCTION

VIMS is most often used to produce spatially resolved spectra of planetary targets between 0.3 and 5.1 μm. However, VIMS is a flexible instrument that can operate in a variety of modes, including an occultation mode (Brown et al. 2004). In this mode, the imaging capabilities are disabled, the short-wavelength VIS channel of the instrument is turned off, and the IR channel obtains a series of 0.8–5.1 μm spectra from a single pixel targeted at a star. Typical sampling intervals were 20–80 ms. The data used in this analysis are uncalibrated, but a mean instrumental thermal background has been subtracted from all the spectra for each occultation. A precise time stamp is appended to every spectrum to facilitate reconstruction of the occultation geometry.

2.1. Observations

Up through the end of 2008, VIMS has observed over 50 occultations, which have yielded a total of 48 potentially useful cuts through the Cassini Division. Table 1 lists the occultation cuts used in this analysis, along with the occultation times and inertial longitudes of the observations, the maximum number of data number (DN) detected, the radial sampling scale, and the shift required to bring circular features into alignment (see below).

2.2. Geometrical Navigation

Table 2 gives the assumed positions of the stars used in this analysis in the International Celestial Reference Frame. For each occultation, the position of the star is adjusted to account for both the proper motion of the star and the parallax at Saturn. The available SPICE kernels provided by the Cassini navigation team were then used to predict the apparent position (radius and inertial longitude) of the star in Saturn's ring plane as a function of time in a planetocentric reference frame, taking into account stellar aberration. In nearly all cases, this estimate of the occultation geometry was confirmed to be accurate to within a few kilometers using the known radii of nearly circular gap edges in the Cassini Division and the outer A Ring (Features 1, 3, 4, 13, 16, and 20 of French et al. 1993). The exceptions were the low-inclination stars *o* Ceti and δ Virginis, for which features could be tens of kilometers away from their nominal positions. In these cases, the fiducial position of Saturn's pole was adjusted slightly (by at most $0\overset{\circ}{.}015$) to bring these cuts into alignment with the other occultations. The residual scatter in the estimated locations of circular features is consistent with uncertainties in the star positions, observation timing, and spacecraft trajectory (see below).

2.3. Light Curve Generation

While each occultation produces several time series of brightness measurements at multiple wavelengths, only the average brightness around a wavelength of 3 μm is used for this analysis. This is because in general, the signal measured by the VIMS instrument was a combination of transmitted starlight and reflected sunlight. The reflected signal from the rings is strongly attenuated at wavelengths close to the strong 2.9 μm water-ice absorption band, so using the spectral channels in this range minimizes the ring background.

To save on data volume, in many of these occultations the normal spectral resolution of the instrument was reduced by a factor of 8. A total of 32 spectral channels were returned with an average resolution $\Delta\lambda \simeq 0.13$ μm. For the few occultations taken at full spectral resolution, the data from the appropriate spectral channels were co-added in software after the fact to make their spectral resolution and signal to noise consistent with the other occultations. For most of the occultations, the summed spectral channel corresponding to the wavelength range between 2.87 and 2.98 μm was used in this analysis. However, a small number of occultations (Rev 13 α Scorpii, Rev 30 R Leonis, Rev 41 α Auriga, Rev 41 R Hydra, and Rev 65 R Cassiopaea), had either sufficiently low signal-to-noise ratios or sufficiently high

Table 1
Occultation Cuts used in this Analysis

Rev	Star	Ingress/ egress	UTC at Jeffreys Gap	Inertial Longitude	max DN at 3 μm	Radial Sampling (km)	Radial Offset (km)	Notes
08	oCet	i	2005-144T05:58	1°	995	0.30	+0.06	A
08	oCet	e	2005-144T07:07	−28°	999	0.30	−0.68	A
13	αSco	i	2005-232T11:46	−70°	860	0.37	+0.77	B,I
13	αSco	e	2005-232T13:44	−3°	770	0.38	−0.98	I
26	αOri	i	2005-204T16:47	−3°	967	0.21	−0.32	
28	αTau	i	2006-252T10:54	34°	144	0.52	+0.15	F
29	δVir	i	2006-268T22:37	204°	125	1.44	−1.35	Xr,A,C
29	δVir	e	2006-268T22:44	97°	128	1.43	+2.74	Xr,A,C
29	αSco	i	2006-269T07:41	−166°	712	0.10	+0.24	
30	RLeo	i	2006-285T02:11	−39°	75	0.44	+0.59	Xd,C,I
30	RLeo	e	2006-285T02:39	−85°	74	0.44	−0.08	Xd,C,I
31	CWLeo	i	2006-301T01:26	−23°	167	3.07	+1.21	Xr,B
31	CWLeo	e	2006-301T02:10	−103°	188	3.07	−0.91	Xr,B
34	αAur	i	2006-336T12:54	27°	414	0.92	+0.21	F
36	RHya	i	2007-001T17:07	−165°	333	0.35	+0.43	B
41	αAur	i	2007-082T17:30	8°	212	0.31	−0.45	B,I
41	RHya	i	2007-088T07:24	−156°	112	0.09	+0.18	B,D,I
63	RLeo	i	2008-094T13:11	96°	368	0.23	+0.93	
63	RLeo	e	2008-094T13:58	126°	371	0.23	+0.01	G
65	RCas	i	2008-112T00:43	30°	77	0.30	+0.27	Xd,C,I
70	CWLeo	i	2008-155T14:22	82°	395	0.76	−2.11	
70	CWLeo	e	2008-155T16:15	137°	363	0.75	−4.15	
71	γCru	i	2008-160T09:04	−173°	422	0.28	+0.46	
72	γCru	i	2008-167T12:21	−174°	639	0.28	+0.83	
73	γCru	i	2008-174T15:30	−174°	635	0.28	+0.46	
75	RLeo	i	2008-191T04:43	80°	279	0.36	+1.07	
75	RLeo	e	2008-191T06:27	138°	279	0.36	−0.63	
77	RLeo	i	2008-205T06:58	84°	295	0.31	+0.10	
77	RLeo	e	2008-205T08:27	133°	296	0.31	+0.18	
78	γCru	i	2008-209T20:07	−175°	304	0.14	+0.52	B
78	βGru	i	2008-210T09:35	−96°	254	0.34	−0.26	
80	RSCnc	i	2008-226T02:03	57°	310	0.56	−0.61	H
80	RSCnc	e	2008-226T07:29	155°	305	0.56	+0.00	
81	γCru	i	2008-231T06:57	−177°	579	0.27	+0.12	
82	γCru	1	2008-238T15:32	−177°	721	0.27	−0.04	
85	RSCnc	i	2008-262T22:29	59°	306	0.54	−0.30	
85	RSCnc	e	2008-263T03:48	153°	312	0.54	+0.31	
86	γCru	i	2008-268T03:12	−178°	1020	0.41	−0.33	
87	RSCnc	i	2008-277T16:16	59°	326	0.53	−0.12	
87	RSCnc	e	2008-277T21:30	152°	325	0.53	+0.01	
89	γCru	i	2008-290T04:23	−178°	704	0.27	−0.13	B
92	RSCnc	i	2008-315T01:56	85°	225	0.21	+0.67	B
93	γCru	i	2008-320T16:31	−157°	484	0.18	+0.09	B,E
94	γCru	i	2008-328T01:23	−168°	267	0.13	+0.30	B,E
94	ϵMus	i	2008-328T08:20	−102°	188	0.19	+0.53	B
94	ϵMus	e	2008-328T13:02	−44°	188	0.19	+0.02	B
96	γCru	i	2008-343T11:45	−172°	236	0.14	+0.18	B
97	γCru	i	2008-351T11:03	−172°	794	0.42	+0.44	

Notes. Times, longitudes, and maximum DN are evaluated inside the Cassini Division. Processing notes: excluded from Cassini-Division analysis due to coarse radial sampling; Xd: excluded from Cassini-Division analysis due to low signal levels; A: low inclination occs, Saturn pole position adjusted to achieve approximate match with circular features; B: data smoothed by three prior to edge-finding; C: data resampled and smoothed by five prior to edge-finding; D: data smoothed by 10 prior to finding Bessel Gap Inner Edge; E: data smoothed by 12 prior to finding Laplace Gap Inner Edge; F: Jeffreys Gap Inner Edge falls in data gap; G: Laplace Ringlet Inner Edge falls in data gap; H: Kuiper Gap Inner Edge falls in data gap; I: spectral channels covering the range from 2.73 to 3.11 μm used.

cosmic-ray fluxes that a single profile was too noisy to obtain reliable edge detections. In these cases, three brightness profiles were averaged together, covering the wavelength range of 2.73–3.11 μm. This simple averaging reduced the instrumental noise and cosmic-ray background to acceptable levels.

While using data near 2.9 μm minimizes the background from the illuminated rings, it does not completely eliminate this signal from all occultations. This residual ring background can be eliminated by comparing data at different wavelengths (Nicholson & Hedman 2009), but such refinements are not necessary here because the goal of this analysis is simply to determine the locations of sharp edges. The time variations in the ring background are limited by the *spatial* resolution of the instrument, while the time variations in the stellar signal

Table 2
Assumed Star Positions in the International Celestial Reference Frame at the *Hipparcos* Epoch

Star	Right Ascension (hr:min:sec)	Declination (hr:min:sec)	Proper Motion R.A. (mas yr^{-1})	Proper Motion Decl. (mas yr^{-1})	Parallax[a] (mas)
oCet	02:19:20.7866	−02:58:37.418	+10.33	−239.48	7.79
αSco	16:29:24.4675	−26:25:55.006	−10.16	−23.21	5.40
αOri	05:55:10.2892	+7:24:25.331	+27.33	+10.86	7.63
αTau	04:35:55.2005	+16:30:35.142	+62.78	−189.36	50.09
δVir	12:55:36.4833	+03:23:51.355	−471.44	−52.81	16.11
RLeo	09:47:33.4907	+11:25:44.020	−0.57	−42.70	9.87
CWLeo	09:47:57.382	+13:16:43.66	...	...	...
αAur	05:16:41.2956	+45:59:56.505	−75.52	−427.13	77.29
RHya	13:29:42.8189	−23:16:52.888	−60.73	+11.01	1.62
RCas	23:58:24.7936	+51:23:19.545	+84.39	+18.07	9.37
γCru	12:31:09.9293	−57:06:45.249	+27.94	−264.33	37.09
ηCar	10:45:03.591	−59:41:04.26	−7.6	+1.0	...
βGru	22:42:39.9349	−46:53:04.437	+135.68	−4.51	19.17
RSCnc	9:10:38.8054	+30:57:47.589	−9.41	−33.05	8.21
ϵMus	12:17:34.6363	−67:57:38.418	−231.26	−26.37	10.80

Notes. Data obtained from the Simbad astronomical database and the *Hipparcos* online catalog. Note that all the stars except CWLeo and ηCar were present in the *Hipparcos* catalog.
[a] Parallax measured at Earth.

are limited by the *temporal* resolution, so the ring background varies slowly with time compared to the variations in the stellar signal and has negligible effect on the inferred locations of sharp edges.

2.4. Edge Detection

After deriving the light curve and geometrically navigating each occultation, we determined the radius, inertial longitude, and time when the star passed behind 22 edges in the Cassini Division: the inner and outer edges of the Huygens, Herschel, Russell, Jeffreys, Kuiper, Laplace, Bessel, and Barnard Gaps, as well as the inner and outer edges of the dense ringlets in the Huygens, Herschel, and Laplace Gaps. Note that we do not consider the "Strange" ringlet in the Huygens Gap in this analysis, nor the low-optical depth ringlets in the Huygens, Jeffreys, or Laplace Gaps.

The edges in the Cassini Division are quite variable in their morphology, and even a single edge may have different shapes in different occultations. This could make the identification of edges based on half-light levels (French et al. 1993) problematic, so instead we identified the edge as the point in the light curve with the steepest slope. Even so, some effort was required to prevent the edge-detection algorithm from mistaking cosmic-ray spikes or other sharp ring features for the desired edge. The algorithm therefore begins by normalizing the total signal (star + reflected ringshine, if any) to unity in the gaps. This is accomplished by first determining the average DN in two clear zones (117,700–117,750 km and 119,970–120,000 km) within the two widest gaps in the Cassini Division: the Huygens Gap and the Laplace Gap. A linear trend based on these two numbers establishes the unocculted stellar brightness throughout this region and is used to normalize the data so that the signal in each gap is approximately 1.0.

For each edge, a fiducial zone is selected for analysis which is sufficiently wide to accommodate all observed edge positions and residual pointing errors. (For the B-ring edge this region is 150 km wide. For the Huygens Ringlet edges this zone is 40 km wide. For the Herschel Ringlet and Herschel Gap inner edge it is 20 km wide. For the inner edge of the Laplace Gap it is 15 km wide. For the Herschel Gap outer edge, the Russell and Jeffreys Gap inner edges, the Laplace Ringlet and the Laplace Gap outer edge, and the Bessel and Barnard Gaps it is 10 km. For the Russell and Jeffreys Gaps' outer edges and the Kuiper Gap edges it is 5 km.) The algorithm first makes a preliminary estimate of the location of the relevant gap edge based on where the signal in this region first deviates significantly from unity. The final estimate of the edge location is then the point where the brightness profile has the steepest slope in a region within ±4 km of the preliminary edge estimate (except for the low-resolution δ Virginis occultation, where a region ±20 km was used).

For certain occultations with fast time sampling or low signal to noise, the raw profile is too noisy for the above algorithm to find all the edges reliably. In these cases, a boxcar smoothing was applied to the data prior to estimating the edge position. The occultations where this was done and the specific smoothing lengths used are given in Table 1. In all cases, the uncertainty in the edge position is determined by the radial sampling interval because this is typically much larger than the projected stellar diameter or the Fresnel zone.

2.5. Occultation Quality

While the above procedure was applied to all the occultation cuts in Table 1, there were a few occultations which we elected not to use with the Cassini-Division edges. The Rev 30 R Leonis and Rev 65 R Cassiopaea occultations had signal-to-noise ratios too low to detect all the edges in the Cassini Division reliably, while the resolution of the Rev 29 δ Virginis and the Rev 31 CW Leonis occultation were so much lower than the rest of the observations that they would not contribute much to our understanding of most of these edges. These data are therefore not considered "Quality" occultations and are not used in the analysis involving the edges within the Cassini Division itself (they are designated with Xr or Xd in Table 1). However, many of these occultations occur at early times in the Cassini mission, when VIMS occultations are comparatively rare, so they are useful when considering the time-evolution of the B-ring edge (see below).

Table 3
Elementary Properties of Cassini-Division Gap Edges

Feature	Mean Radius (km)	St. Dev. (km)	Edge Type
B-ring Outer Edge	117564.4	51.4	Resonant (2:1 Mimas)
Huygens Ringlet Inner Edge	117804.4	20.3	Eccentric
Huygens Ringlet Outer Edge	117822.8	20.2	Eccentric
Huygens Gap Outer Edge	117930.6	2.8	Unknown
Herschel Gap Inner Edge	118188.2	5.9	Eccentric
Herschel Ringlet Inner Edge	118233.9	2.3	Unknown
Herschel Ringlet Outer Edge	118263.2	2.7	Unknown
Herschel Gap Outer Edge	118283.4	1.1	Unknown (Circular?)
Russell Gap Inner Edge	118589.7	5.2	Eccentric
Russell Gap Outer Edge	118628.2	0.9	Circular
Jeffreys Gap Inner Edge	118929.6	2.7	Eccentric
Jeffreys Gap Outer Edge	118966.5	0.8	Circular
Kuiper Gap Inner Edge	119401.7	1.0	Eccentric
Kuiper Gap Outer Edge	119406.1	0.7	Circular
Laplace Gap Inner Edge	119845.2	2.6	Eccentric
Laplace Ringlet Inner Edge	120036.4	1.8	Unknown (Resonant? 9:7 Pandora)
Laplace Ringlet Outer Edge	120077.7	2.1	Eccentric
Laplace Gap Outer Edge	120085.7	1.3	Eccentric
Bessel Gap Inner Edge	120231.3	1.6	Eccentric
Bessel Gap Outer Edge	120243.6	1.0	Circular?
Barnard Gap Inner Edge	120303.7	2.4	Resonant? (5:4 Prometheus)
Barnard Gap Outer Edge	120315.9	0.7	Circular

3. DATA ANALYSIS

The above procedures yield roughly 40 "quality" estimates of the position of each of the 22 selected gap edges for a range of different times and inertial longitudes. The simplest statistics that can be computed from these data are the (unweighted) means and standard deviations of all the edge estimates, which are presented in Table 3. Of particular interest are the standard deviations, which range from around 1 km up to 50 km for the edge of the B ring.

Based on these variances, we can begin to identify several different classes of edges in the Cassini Division. First of all, there are several features whose scatter is around 1 km, which likely represent truly circular ring edges. These include the outer edges of the Russell, Jeffreys, Kuiper, Barnard, and possibly the Bessel and Herschel Gaps. (The inner edge of the Kuiper Gap has a similarly low variance, but further investigation shows that it belongs in the eccentric class of ring features, discussed below).

The remaining edges all have noticeably larger variances and therefore appear to be non-circular in some form. Three of these edges (the outer edge of the B ring, and the inner edges of the Laplace Ringlet and the Barnard Gap) are close to mean-motion resonances with known satellites of Saturn (Mimas 2:1, Pandora 9:7 and Prometheus 5:4, respectively) which could provide natural explanations for their shapes. However, this still leaves most of the edges unexplained. We have found that 10 of these features (both edges of the Huygens Ringlet, the inner edges of the Herschel, Russell, Jeffreys, Kuiper, Laplace, and Bessel Gaps, and the outer edges of the Laplace Gap and Ringlet) can be well fit with ellipses that precess around the planet at the expected rate given Saturn's oblateness. Four non-circular edges (both sides of the Herschel Ringlet, as well as the outer edges of the Huygens and possibly the Herschel Gaps) cannot be fit by simple elliptical models and therefore require further investigation.

We will consider each of these different classes in detail below. First, we will investigate the apparently circular edges and show how they can be used to refine the estimates of the other edge locations. Next, we will discuss the eccentric features and compare the amplitudes and precession rates of these features. We will then consider the inner edge of the Barnard Gap and explore whether the structure of this edge can be explained by the perturbations from Prometheus. Finally, we will look at the outer edge of the B ring, which has the largest radial excursions and the most complex structure. The inner edge of the Laplace Ringlet, both edges of the Herschel Ringlet, and the outer edges of the Herschel and Huygens Gaps still require further study and will not be discussed in detail in this paper.

3.1. Circular Edges

Figure 2 shows the scatter in the inferred positions of the outer edges of the Herschel, Russell, Jeffreys, Kuiper, Bessel, and Barnard Gaps. All of these data sets have rather low dispersions. Furthermore, there is a strong correlation among the radial excursions of different edges from the same occultation. (For example, the low points in all six panels near 80° and 140° longitude come from the Rev 70 CW Leo occultations. Since this object was not observed by *Hipparcos*, the occultation geometry here is more uncertain than the others.) This suggests that most of the scatter in the positions of these edges is due to small errors in the geometric reconstructions of different occultations.

Assuming that most of these edges are circular, we use these features to compute a radial offset for each cut and refine the location estimates for the remaining edges. For each occultation, we compute the mean deviation of the measured positions of the outer edges of the Russell, Jeffreys, Kuiper, Bessel, and Barnard Gaps from the mean values listed in Table 3 (118628.2, 118966.5, 119406.1, 120243.6, and 120315.9 km, respectively). These radial shifts, tabulated in Table 1, are then applied to all edges for that occultation. Note that the nominal positions of the

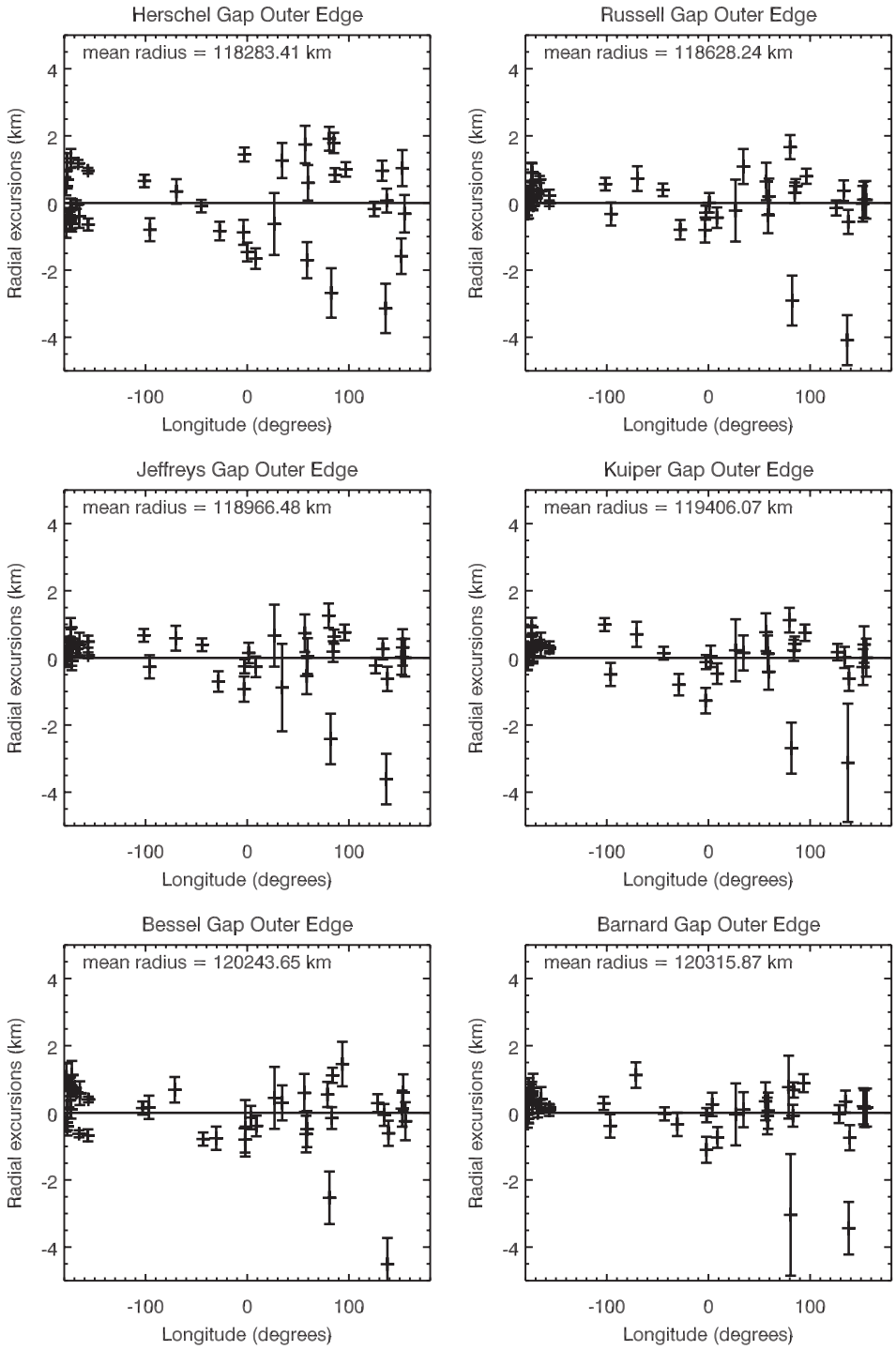

Figure 2. Radial excursions (deviations from the unweighted mean) of six apparently circular edges in the Cassini Division, plotted as functions of inertial longitude. The error bars indicate the radial sampling scale of each occultation.

outer edges of the Russell, Jeffreys, and Bessel Gaps are 1–2 km interior to the values reported in French et al. (1993). Such a small shift should be of no major consequence for this analysis, but will be the subject of a future investigation of Saturn's pole orientation incorporating data from all circular features in the rings.

3.2. Eccentric Edges

The observed radial position r' of an eccentric edge depends on the inertial longitude λ and time relative to some epoch δt of the observation as follows:

$$r' = r'_o - A \times \cos(\lambda - \Omega_p \delta t - \lambda_o), \quad (1)$$

where r'_o is the mean edge location, A is the amplitude of the radial excursions, λ_o is a phase offset, and Ω_p is a pattern speed. Since an eccentric edge closely follows the path of a freely precessing particle on an eccentric orbit, we expect $\Omega_p = \dot{\varpi}$, where $\dot{\varpi}$ is the apsidal precession rate, which in the Cassini Division ranges between $4\overset{\circ}{.}5$ day^{-1} and $5\overset{\circ}{.}1$ day^{-1}.

Preliminary investigations showed that 10 of the edges in the Cassini Division could be well fit by such an eccentric

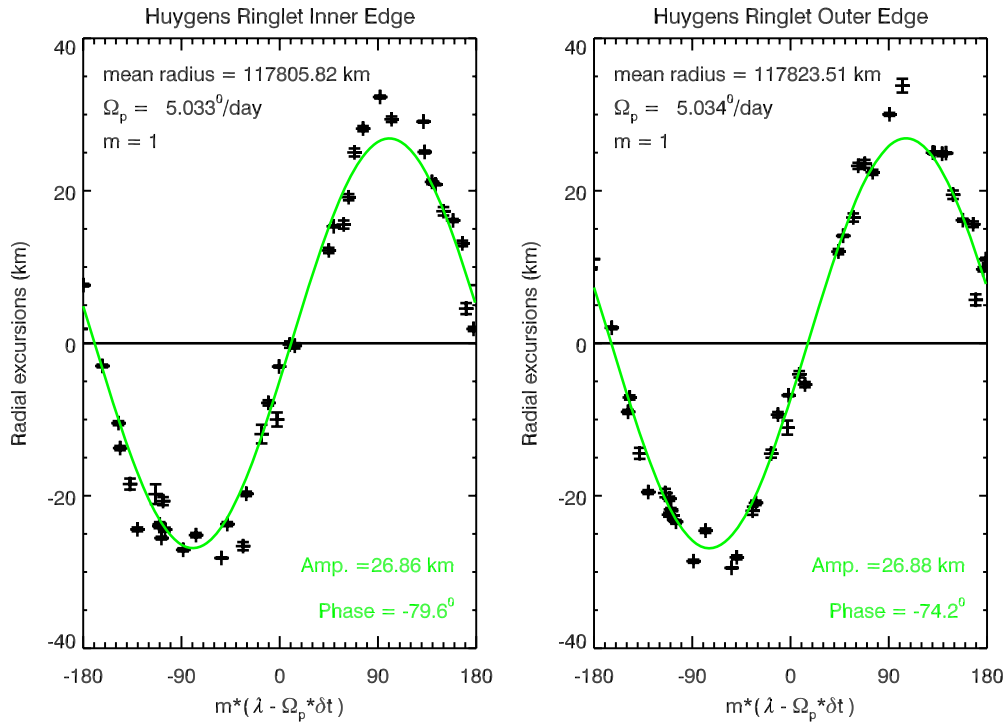

Figure 3. Radial excursions (after offset subtraction) of the inner and outer edges of the Huygens Ringlet. Error bars indicate the radial sampling scales of the different occultations. Note time is measured relative to an epoch of 2005-195T02:13:13.557 (which corresponds to a Cassini spacecraft clock time of 150000000), and the mean radii are for the eccentric model rather than the data.

(A color version of this figure is available in the online journal.)

model with Ω_p close to the expected value of $\dot{\varpi}$. These features are both edges of the Huygens Ringlet, the inner edges of the Herschel, Russell, Jeffreys, Kuiper, Laplace, and Bessel Gaps, as well as the outer edges of the Laplace Gap and Ringlet. The Huygens Ringlet was previously known to be an eccentric structure (Turtle et al. 1991; Spitale & Porco 2006), and there was some evidence that the inner edge of the Herschel Gap might be as well (Flynn & Cuzzi 1989). However, the fact that a majority of the edges in the Cassini Division are simple ellipses is a rather unexpected finding.

Having identified these features, we sought to determine the parameters in Equation (1). Given the extensive occultation data available, and mindful that the precise precession rates at a given location might be affected by nearby ring material (Nicholson & Porco 1988), we chose not to assume a predicted pattern speed for each edge but instead included Ω_p as a free parameter in each fit.

For each possible value of the pattern speed Ω_p, we computed the following quantities:

$$\alpha_R = \frac{1}{n}\sum_{i=1}^{n}(r_i' - \bar{r}') \times \cos(\lambda_i - \Omega_p \delta t_i), \quad (2)$$

$$\alpha_I = \frac{1}{n}\sum_{i=1}^{n}(r_i' - \bar{r}') \times \sin(\lambda_i - \Omega_p \delta t_i), \quad (3)$$

where $\bar{r}'$ is the mean radius of the edge and the sums are over the ~40 measurements of r'. If the radial position of the edge is described by Equation (1), then $\sqrt{\alpha_R^2 + \alpha_I^2} = \rho A/2$, where ρ is the correlation coefficient between $r_i' - \bar{r}'$ and $\cos(\lambda_i - \Omega_p \delta t_i - \lambda_o)$. This function will be at a maximum when there is perfect correlation between these parameters (i.e., when $\rho = 1$). In the limit of perfect sampling of all possible true anomalies ($\lambda_i - \Omega_p \delta t_i$), this should only occur when the assumed pattern speed $\Omega_p$equals the true pattern speed. Thus, the value of $\Omega_p$that yields the highest value of $\sqrt{\alpha_R^2 + \alpha_I^2}$ provides the best estimate of the true pattern speed. In this case, the parameters α_R and α_I will approach $-(A/2)\cos\lambda_o$ and $-(A/2)\sin\lambda_o$(again in the limit of perfect sampling of all possible true anomalies), so we can estimate the amplitude and phase parameters using the equations $A/2 = \sqrt{\alpha_R^2 + \alpha_I^2}$ and $\tan\lambda_o = \alpha_I/\alpha_R$.

Figures 3–5 show the measured radial excursions for the eccentric edges as a function of $\lambda - \Omega_p \delta t$ using the best-fit pattern speeds. In all cases, the data are well organized into a sine wave. Table 4 lists the best-fit parameters for these edges. Note that the observed pattern speeds of these features are not far from the predicted pattern speeds derived by assuming the edge follows a freely precessing elliptical orbit. The uncertainty in the observed pattern speeds is set by the time baseline of the observations, which is approximately 1300 days. A difference of $0\overset{\circ}{.}01$ day^{-1} in the pattern speed would therefore shift the phase of the first and last occultations by roughly 15°, which is probably on the edge of detectability.

What is particularly interesting about the fitted pattern speeds of the eccentric edges is that they almost form a regular sequence. To see this, first note that both edges of the Huygens Ringlet have the same pattern speed ($5\overset{\circ}{.}03$ day^{-1}), as expected for a narrow ringlet, and that all the eccentric features in the Laplace Gap also have similar pattern speeds ($4\overset{\circ}{.}72$ day^{-1}), so there are only seven distinct pattern speeds in Table 4, one for each gap/ringlet. The average difference in pattern speed between adjacent features is $0\overset{\circ}{.}06$ day^{-1}, with a standard deviation of about $0\overset{\circ}{.}01$ day^{-1}, which is comparable to the

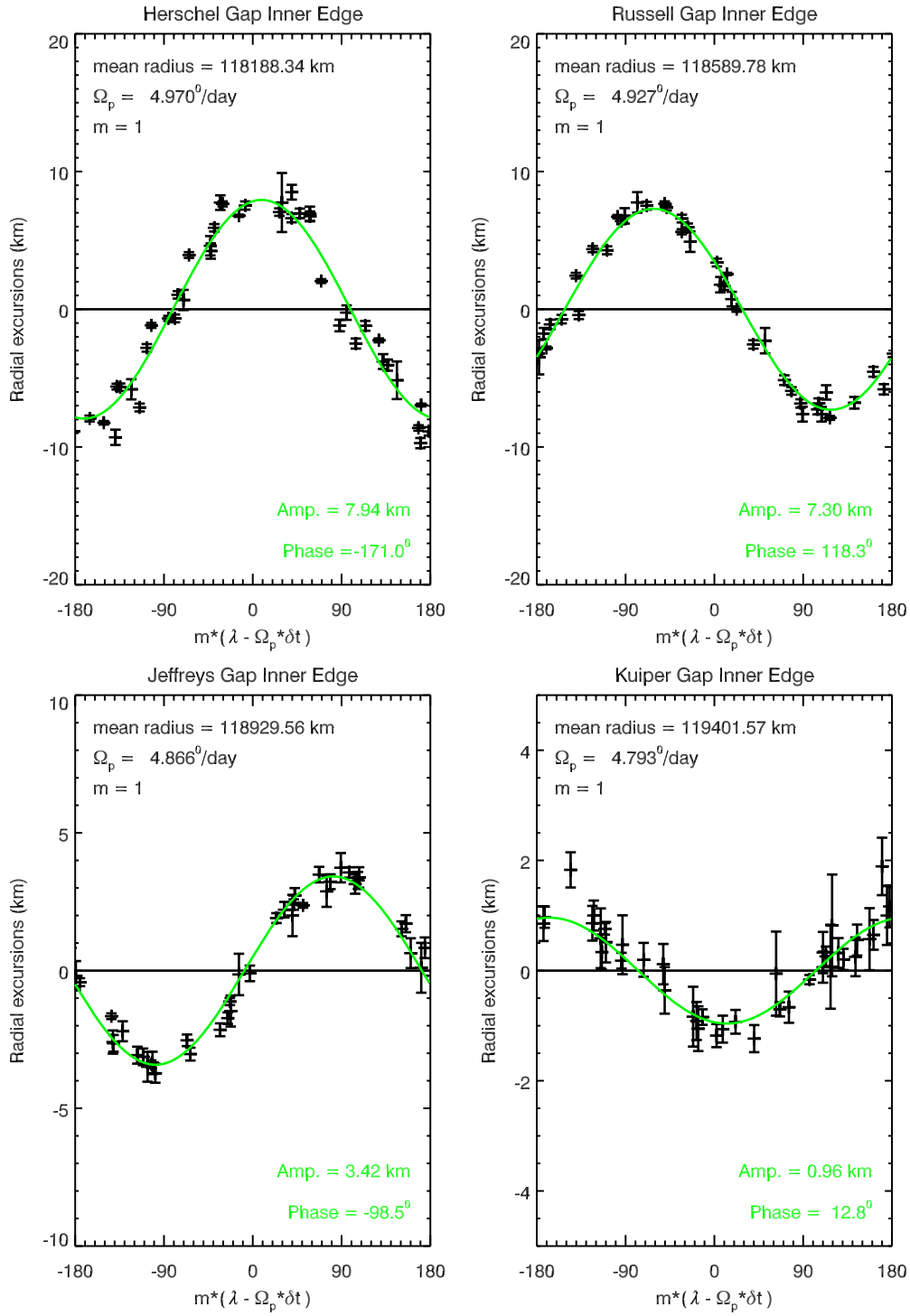

Figure 4. Radial excursions (after offset subtraction) of the inner edges of the Herschel, Russell, Jeffreys, and Kuiper Gaps. Error bars indicate the radial sampling scales of the different occultations. Note time is measured relative to an epoch of 2005-195T02:12:13.557 (which corresponds to a Cassini spacecraft clock time of 150000000), and the mean radii are for the eccentric model rather than the data.

(A color version of this figure is available in the online journal.)

uncertainty in the precession rates of the patterns (outliers being the $0\overset{\circ}{.}04$ day^{-1} difference between the pattern speeds for the Herschel and Russell Gap inner edges and the $0\overset{\circ}{.}08$ day^{-1} difference between the Jeffreys and Kuiper Gap inner edges). Also, with the exception of the almost-circular Kuiper Gap inner edge, there is an almost monotonic decrease in the amplitude of these patterns from 27 km at the Huygens Ringlet to 2 km at the Bessel Gap. This regularity hints that these eccentric edges may be controlled by a series of closely spaced resonances. This idea will be explored in more detail below after a consideration of the structure of two resonantly controlled edges.

3.3. Barnard Gap Inner Edge

The Barnard Gap inner edge is a special case because it is the only inner edge of a gap in the Cassini Division besides the B-ring edge that cannot be fit to a simple eccentric model.

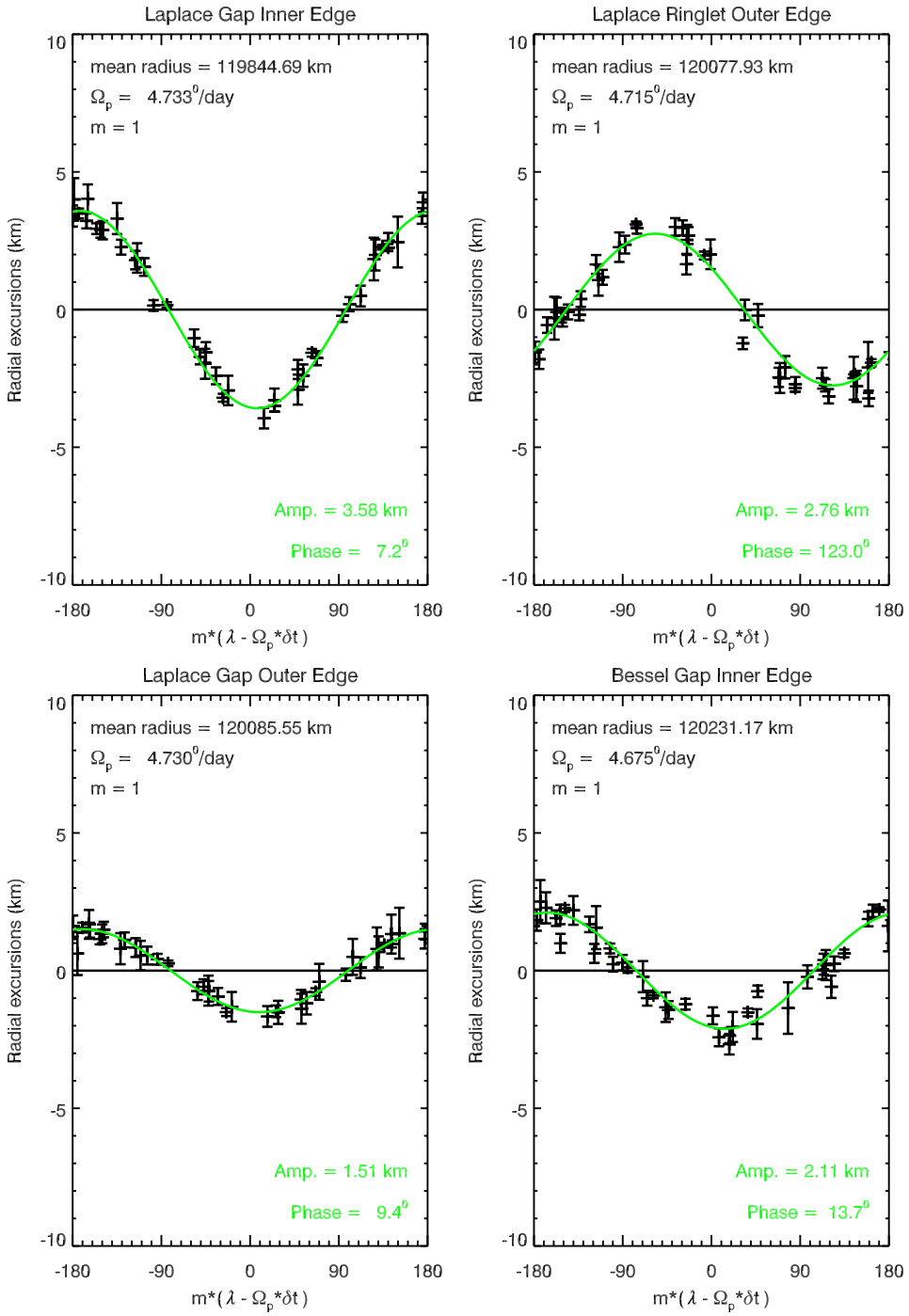

Figure 5. Radial excursions (after offset subtraction) of the inner edges of the Laplace and Bessel Gaps, as well as the outer edges of the of the Laplace Gap and Ringlet. Error bars indicate the radial sampling scales of the different occultations. Note time is measured relative to an epoch of 2005-195T02:12:13.557 (which corresponds to a Cassini spacecraft clock time of 150000000), and the mean radii are for the eccentric model rather than the data.

(A color version of this figure is available in the online journal.)

All the other non-circular, non-eccentric edges are either on ringlets within the gaps (Herschel and Laplace) or at the outer edges of gaps containing such ringlets (Huygens and Herschel). Furthermore, the mean radius of the Barnard Gap's inner edge is 120304 km, which is very close to the predicted location of the Prometheus 5:4 inner Lindblad resonance (ILR) at 120303.7 km. Thus, it is reasonable to expect that the shape of this edge is described by the following function:

$$r = r_o - A \times \cos(5(\lambda - \lambda_{\rm Prometheus})). \quad (4)$$

Figure 6 plots the radial excursions of this edge as a function of $5(\lambda - \lambda_{\rm Prometheus})$, and indeed shows that most of the data can be roughly described by the above functional form. There are some clear deviations from the expected pattern, most noticeably some points with large positive excursions near $5(\lambda - \lambda_{\rm Prometheus}) = 20^\circ$, and a possible phase shift in the data relative to the model. Similar deviations are seen in the B-ring edge as well (see below), and may reflect complications in the dynamics of resonantly controlled edges. In spite of this, it does appear that the Barnard Gap is strongly influenced, and probably controlled, by the 5:4 Lindblad resonance with Prometheus.

Table 4
Parameters for the Eccentric Edges

Feature	Mean Radius[a]	Amplitude	Phase[b]	Pattern Speed (Observed)	Pattern Speed (Predicted)[c]
Huygens Ringlet Inner Edge	117805.8 km	26.9 km	−80°	5.°03 day^{-1}	5.°022 day^{-1}
Huygens Ringlet Outer Edge	117823.5 km	26.9 km	−74°	5.°03 day^{-1}	5.°019 day^{-1}
Herschel Gap Inner Edge	118188.3 km	7.9 km	−171°	4.°97 day^{-1}	4.°964 day^{-1}
Russell Gap Inner Edge	118589.8 km	7.3 km	118°	4.°93 day^{-1}	4.°904 day^{-1}
Jeffreys Gap Inner Edge	118929.6 km	3.4 km	−98°	4.°87 day^{-1}	4.°854 day^{-1}
Kuiper Gap Inner Edge	119401.6 km	1.0 km	13°	4.°79 day^{-1}	4.°786 day^{-1}
Laplace Gap Inner Edge	119844.7 km	3.6 km	7°	4.°73 day^{-1}	4.°723 day^{-1}
Laplace Ringlet Outer Edge	120077.9 km	2.8 km	123°	4.°72 day^{-1}	4.°691 day^{-1}
Laplace Gap Outer Edge	120085.6 km	1.5 km	9°	4.°73 day^{-1}	4.°689 day^{-1}
Bessel Gap Inner Edge	120231.2 km	2.1 km	14°	4.°68 day^{-1}	4.°669 day^{-1}

Notes.
[a] Note these mean radii differ slightly from those in Table 3 because these are the mean radii of the eccentric model rather than the mean of the data.
[b] Longitude of edge's pericenter for an eccentric model using the given pattern speed at an epoch of 2005-195T02:12:13.557 (which corresponds to a Cassini spacecraft time of 150000000).
[c] Predicted precession rate of eccentric particle orbit with semimajor axis equal to the observed mean edge radius, based on current estimates of Saturn's gravity field parameters (Jacobson et al. 2006).

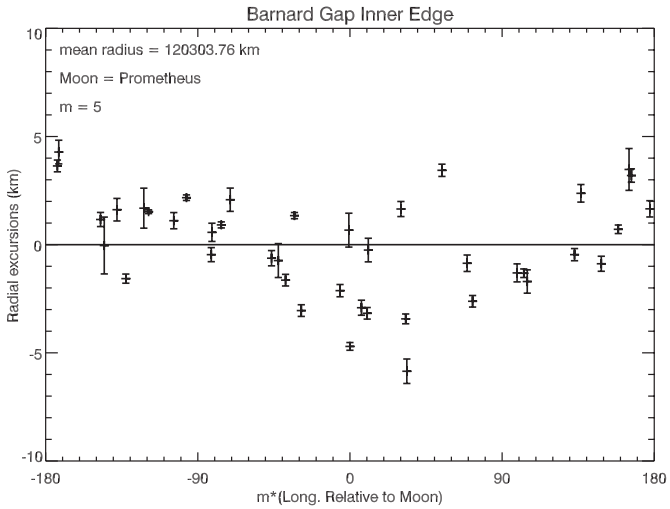

Figure 6. Radial excursions of the inner edge of the Barnard Gap, plotted as a function of five times the longitude relative to Prometheus. Note that the data are reasonably well organized in this longitude system, consistent with the edge being influenced by the 5:4 resonance with Prometheus.

3.4. B-ring Outer Edge Observations

The outer edge of the B ring has long been known to be strongly affected by the Mimas 2:1 ILR (Goldreich & Tremaine 1978; Smith et al. 1982). The radial excursions of a particle's orbit near this resonance can be described by the following equation (see Section 4 below):

$$r = r_o - A \times \cos(2(\lambda - \lambda_{\rm Mimas})). \quad (5)$$

Analyses of the *Voyager* data showed that the above expression provided a reasonably accurate description of the outer edge of the B ring in 1981 with an amplitude $A \simeq 75$ km (Porco et al. 1984). However, as shown in the top panel of Figure 7, the VIMS occultation data do not fit this simple model so clearly. The measurements obtained in 2008 do possess a clear $m = 2$ structure with an amplitude of 75 km, but there is a significant phase offset, such that the minimum radius does not occur where $\lambda \simeq \lambda_{\rm Mimas}$ but instead lags behind this point by about 40° in phase (i.e., one of the two minima falls ∼20° in longitude behind Mimas). Furthermore, the data taken prior to 2008 fall well away from the curve described by the 2008 data. The radial differences between the 2005–2007 and 2008 data are as much as 100 km, which is far too large to be explained by pointing errors, time variability in the pattern's amplitude or some additional (smaller amplitude) perturbations in the edge position. Instead, the differences between the 2005–2007 data and the 2008 data are best explained by a time variation in the orientation of the pattern relative to Mimas. Indeed, if we assume the pattern moves at a speed ∼0.°045 day^{-1} slower than Mimas' mean motion, then the 2005–2007 data are well aligned with the 2008 data (see the bottom panel of Figure 7). It therefore appears that between 2005 and 2008 the phase of this $m = 2$-symmetric pattern has drifted backwards relative to Mimas.[7]

This trend in the pattern's orientation over the last few years can also be detected by comparing the VIMS occultation data obtained in 2008 with various measurements of the B-ring edge made by other instruments earlier in the Cassini Mission. Data from 12 occultations of the radio signal from the Cassini spacecraft (French et al. 2009) confirm that in 2005 the $m = 2$ radial excursions of the B-ring edge led Mimas by 70° in phase (or 35° in longitude). A similar result was obtained by Spitale & Porco (2006), based on Cassini imaging sequences in 2005. The pattern has therefore drifted backwards relative to Mimas by ∼55° in longitude (or 110° in phase) between 2005 and 2008, consistent with the drift rate obtained using the VIMS data alone.

A steady drift in the $m = 2$ pattern relative to Mimas would be extremely surprising, given that this pattern is supposed to be generated by gravitational perturbations from that moon. It seems more reasonable that the orientation of the $m = 2$ pattern instead librates relative to the moon on a timescale that is long compared to the Cassini mission to date. We therefore posit that

[7] The long-term average mean motion of Mimas is 381.°994509 ± 0.°000005 day^{-1} (Harper & Taylor 1993), but the 4:2 resonance with Tethys results in a slow variation in the mean motion with an amplitude of 0.°011 day^{-1} and a period of 70.8 years. Although this variation is too small to account for the observed drift in the B-ring edge distortion, it does lead to an instantaneous mean motion at epoch (Day 2005-195) of 381.°984 day^{-1}, close to that derived from the JPL SPICE ephemeris.

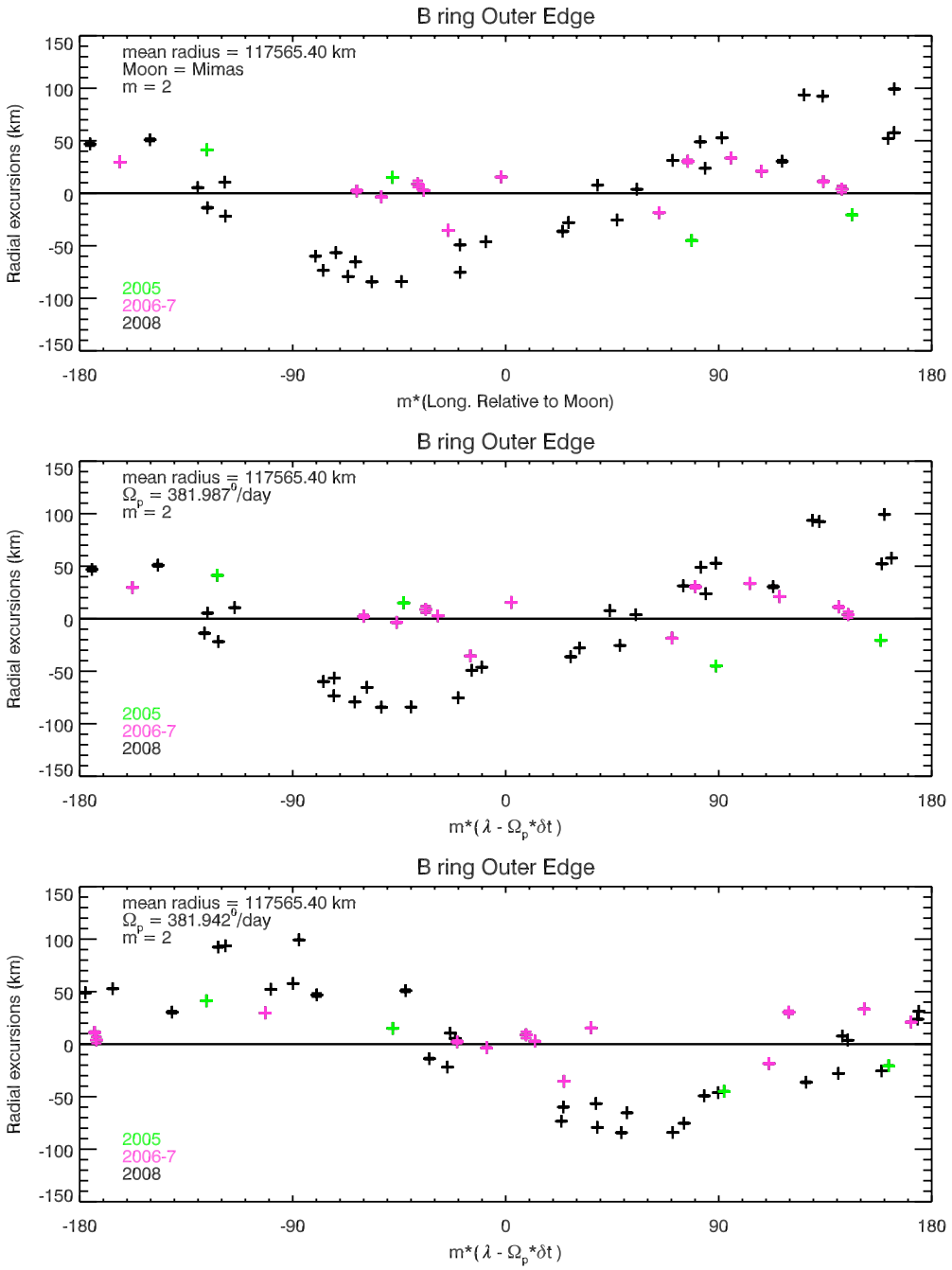

Figure 7. Radial excursions of the outer edge of the B ring. The top panel shows the data plotted vs. the difference in longitude relative to Mimas. The middle panel shows the data assuming a constant pattern speed equal to Mimas' mean motion, and the bottom panel shows the data organized using a slightly slower pattern speed that provides the best fit to the data. Note that data from all 48 occultation cuts in Table 1 are used in these plots.

(A color version of this figure is available in the online journal.)

the $m = 2$ structure of the B-ring edge can be described by the following equation:

$$r = r_o - A \times \cos(2[\lambda - \lambda_{\rm Mimas} - \phi_L \times \sin(Lt - \theta_L)]), \quad (6)$$

where the last term in the cosine argument describes a slow libration of the longitude of the minimum radius relative to Mimas with an amplitude of ϕ_L and a period of $2\pi/L$ (we shall see below that the amplitude A also appears to be time dependent).

Estimating ϕ_L and L from the Cassini VIMS data alone is difficult because the libration period appears to be significantly longer than the observation arc. Earlier measurements of the B-ring edge orientation back to the *Voyager* missions could be useful, but these data are rather sparse, so before we consider using those data, it is useful to first place some constraints on the libration parameters using the Cassini VIMS data alone.

Since the pattern probably aligned with Mimas sometime during 2007, we can make the crude approximation that during the entire Cassini mission to date $\sin(Lt - \theta_L) \simeq (Lt - \theta_L)$, in which case

$$r \simeq r_o - A \times \cos(2[\lambda - (n_{\rm Mimas} + \phi_L L)t + \phi_L \theta_L - \lambda_{\rm Mimas}(t = 0)]), \quad (7)$$

where $n_{\rm Mimas} \simeq 381.^{\circ}99$ day^{-1} is the current mean motion of Mimas. In this case, the same basic procedure described above

for finding the pattern speeds of the eccentric edges can be used to estimate the value of $n_{\rm Mimas} + \phi_L L$ that best fits the data. Using all the VIMS occultation data, the best-fit pattern speed for the $m = 2$ component of the B-ring edge is found to be 381.°945 day^{-1}, or about 0.°045 day^{-1} slower than Mimas' mean motion (see Figure 7, bottom panel; using only the quality data or including the radio science data does not change this result much). Thus, the product $|\phi_L L|$ must be 0.°045 day^{-1} (where ϕ_L is measured in radians and L is measured in degrees day^{-1}).

To turn this estimate of $|\phi_L L|$ into a constraint on L, note that ϕ_L cannot have any value. First, ϕ_L cannot exceed 90° or else the pattern would be circulating instead of librating, which seems unlikely. Also, ϕ_L is probably at least 35° or 0.6 rad, since the pattern is offset by that much in 2005. These considerations suggest that L most likely lies somewhere in the range between 0.°03 day^{-1} and 0.°10 day^{-1}, corresponding to a libration period of between 10 and 30 years.

Additional rough constraints on ϕ_L and L can be obtained by recalling that analyses of the *Voyager* data showed that the $m = 2$ pattern was aligned with Mimas in 1980–1981 (Porco et al. 1984). This suggests that zero-crossings of the libration occurred in 1980–1981 and 2007, which would imply the libration period is a submultiple of 52 years, or that L is an integral multiple of 0.°02 day^{-1}. The Cassini-based estimate of $|\phi_L L|$ and the *Voyager* data can be satisfied if $L \simeq 0.°04$ day^{-1}, 0.°06 day^{-1}, 0.°08 day^{-1}, etc. (with $\phi_L \simeq 60°$, 40°, and 30°, etc., respectively).

Guided by these constraints, we performed a more comprehensive investigation of the B-ring edge using a combination of occultation data obtained over the last 30 years. This combined data set includes (1) the 48 VIMS occultation cuts listed in Table 1, (2) 12 occultation cuts from 2005 obtained by the Cassini radio-science experiment (RSS) reported in French et al. (2009) and kindly provided to us, (3) the *Voyager 1* RSS occultation (Tyler et al. 1983), (4) the *Voyager 2* PPS occultation (Lane et al. 1982; Esposito et al. 1983, 1987), (5) multiple data from the ground-based 28 Sagittarius occultations from 1989 July (French et al. 1993), and (6) occultations observed by the *Hubble Space Telescope* in 1991 (Elliot et al. 1993) and 1995 (Bosh et al. 2002). All of the pre-Cassini data have been re-analyzed by French et al. (2009).

To determine which combination of libration parameters could best fit these data, we computed the Pearson's correlation coefficient ρ between the radial excursions and the parameter $\cos(2[\lambda - \lambda_{\rm Mimas} - \phi_L \times \sin(Lt - \theta_L)])$ for different values of ϕ_L, L, and θ_L. This correlation coefficient will be maximal with the model parameters that best match the actual motion of the edge, so it provides a convenient way to search the parameter space for likely solutions. This method also has the advantage that it is relatively insensitive to any time variability in the amplitude A of the pattern (see below).

Based on this analysis, we found that solutions with $L <$ 0.°05 day^{-1} were strongly disfavored. This is primarily because all of the pre-Cassini measurements show negative radial excursions, and there was no way to align both the 28 Sgr and *Voyager* measurements with the minima in the Cassini data unless $L >$ 0.°05 day^{-1}. Furthermore, we found that frequencies near 0.°058 day^{-1} and 0.°117 day^{-1} better organized the data than other frequencies. Note that both these frequencies are part of the acceptable series of values that the above simplistic analysis suggested would be compatible with both the *Voyager* and Cassini data.

Unfortunately, the available data do not clearly favor one of these two solutions for the B-ring edge over the other. The top two panels in Figure 8 show the two best-fit solutions, with libration frequencies 0.°058 day^{-1} and 0.°117 day^{-1} and libration amplitudes $\phi_L = 52°$ and 32° (in both cases the most recent zero-crossing time was in mid-2007). The scatter of the data about the mean curves is not significantly different in these two cases, so both solutions are equally good in this respect. Worse, the earlier data are unable to rule out the possibility that the $m = 2$ pattern could be drifting backwards at a constant speed instead of librating. The bottom panel of Figure 8 shows the data plotted using the best-fit constant pattern speed, which turns out to be 381.°932 day^{-1}, or about 0.°05 day^{-1} slower than Mimas' current mean motion. The scatter in the data for this solution is not much larger than it is for the librating solutions.

Future observations may eventually provide a way to discriminate between these possible solutions. However, some of the difficulty in determining the correct model for the motion of the $m = 2$ pattern stems from the comparatively large scatter in the measurements with respect to any of the above solutions. In all cases, the average amplitude of the pattern is around 60 km, but rms residuals are roughly 20 km, which is much larger than the ∼1 km measurement errors in each of these data sets. This suggests that the B-ring edge is not just a fixed-amplitude $m = 2$ pattern that librates relative to Mimas, but has a more complex shape, perhaps with additional perturbation modes.

To explore this possibility, let us take a closer look at two particular subsets of the data: the VIMS data from 2008 and the combined VIMS and RSS data from 2005. Each of these subsets consists of a reasonably large number of occultation cuts (31 and 16, respectively) that were not only taken over a sufficiently broad range of longitudes relative to Mimas that we can estimate the shape of the $m = 2$ pattern, but also obtained in a sufficiently short period of time that we can ignore the libration of the pattern with respect to Mimas.

The best-fit $m = 2$ pattern for the 2008 data has an amplitude of 75.3 km and a phase of −39.°4 relative to Mimas (i.e., the pattern lags Mimas by 19.°7 in longitude), while the best-fit pattern for the 2005 data has an amplitude of 48.7 km and a phase of +70.°0. Thus, the amplitude of the $m = 2$ pattern varies with time as well as the phase (see Figure 9). This is not entirely unexpected, given that a libration can often be modeled as a combination of free and forced terms, which naturally leads to coupled variations in both the phase and the amplitude of the pattern (see Section 4 below). Indeed, some of the observed scatter in the data in Figure 8 is likely due to unmodeled changes in the amplitude of the $m = 2$ pattern. Even so, the variations in the amplitude of the pattern cannot be the only source of scatter in these data, as each of the 2008 and 2005 data sets alone show significant scatter around the mean $m = 2$ pattern, with individual residuals up to ∼40 km (see Figure 9).

A previous analysis of Cassini images by Spitale & Porco (2006) suggested that additional perturbations, possibly $m = 3$, might influence the B-ring edge's shape. Motivated by this result, we took the 2008 and 2005 data sets, removed the best-fitting $m = 2$ pattern from each of them, and fitted the residuals to $m = 0$, 1, 3, 4, 5, and 6 patterns. For each non-zero value of m, we examined a range of pattern speeds in the vicinity of the expected speed of a "normal mode" (French et al. 1991) with this m number:

$$\Omega_p = [(m-1)n + \dot{\varpi}]/m. \quad (8)$$

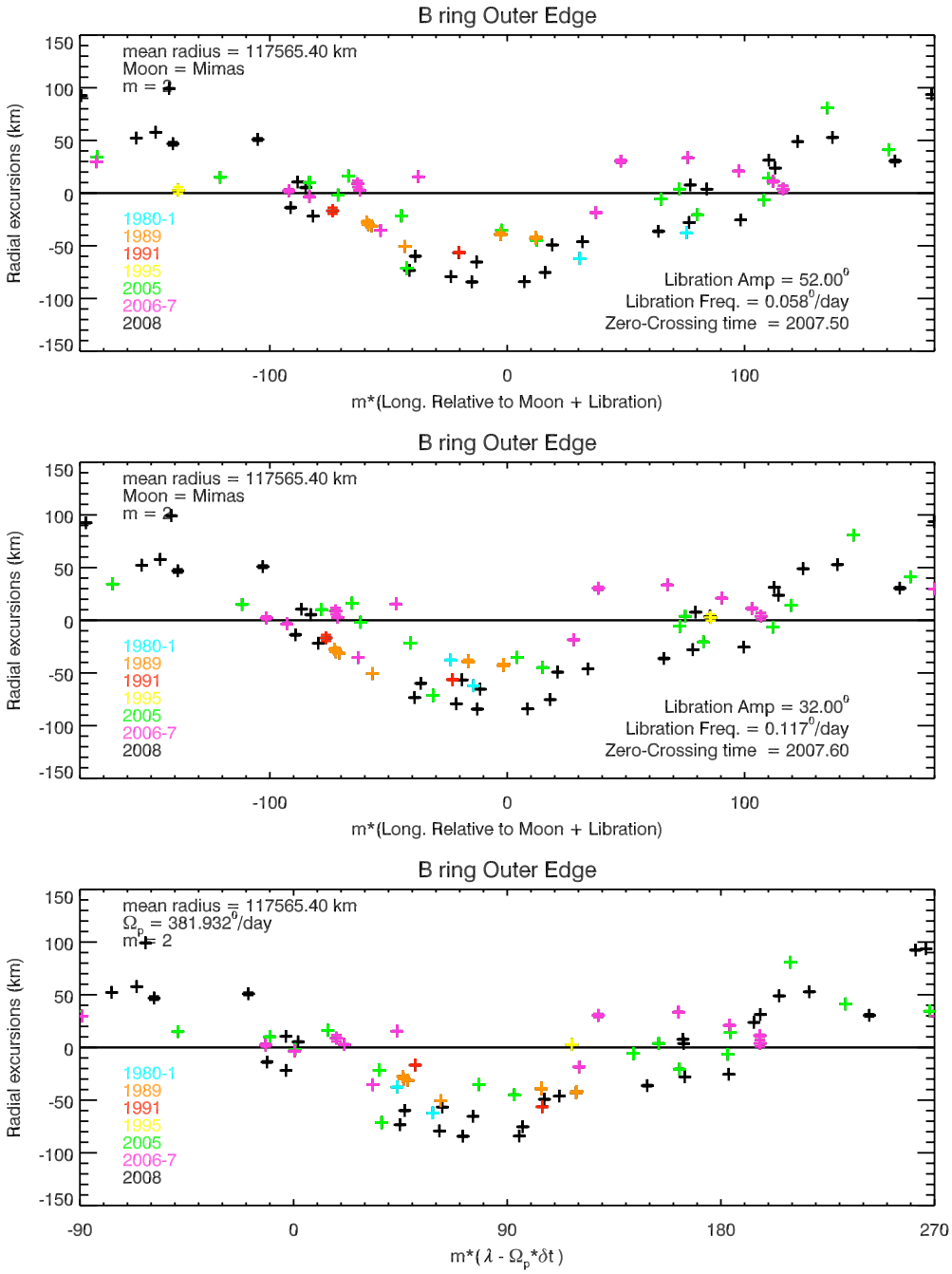

Figure 8. Radial excursions of the B-ring edge, including data from Cassini-VIMS and RSS experiments, *Voyager* observations and various earth-based occultation observations. The top two panels show the data as organized using a librating longitude system with libration frequencies of 0.°058 day^{-1} and 0.°117 day^{-1}, respectively. The bottom panel shows the data organized using a steady drift rate of $\sim$0.°05 day^{-1} slower than Mimas' mean motion (as before, times are measured relative to an epoch of 2005-195T02:12:13.557 or a Cassini spacecraft clock time of 150000000). The available data are clearly insufficient to distinguish between these different models, given the very large residual scatter.

For $m = 0$, the pattern does not rotate, but the whole ring oscillates radially at the epicyclic frequency $\kappa = n - \dot{\varpi}$, as observed for the Uranian γ ring (French et al. 1986). As with eccentric features in the Cassini Division, we computed the amplitudes

$$\alpha_R = \frac{1}{n}\sum_{i=1}^{n} \delta r_i \times \cos[m((1-\delta_{m0})\lambda_i - \Omega_p \delta t_i)], \quad (9)$$

$$\alpha_I = \frac{1}{n}\sum_{i=1}^{n} \delta r_i \times \sin[m((1-\delta_{m0})\lambda_i - \Omega_p \delta t_i)], \quad (10)$$

where δr_i are the residual radial variations in the edge positions after removing the $m = 2$ pattern. As before, if there is a pattern in these radius measurements with a given m and Ω_p, then $\sqrt{\alpha_R^2 + \alpha_I^2}$ should have a maximum at the appropriate values for those parameters.

For both the 2005 and 2008 data sets, the clearest maxima were obtained with $m = 1$. Indeed, as shown in Figure 10, the residuals in the 2008 data are reasonably well fit by a precessing Keplerian ellipse with an amplitude of about 18 km and a pattern speed of 5.°08 day^{-1} (with an uncertainty of $\sim$0.°05 day^{-1} determined by the $\sim$6-month observing arc). This

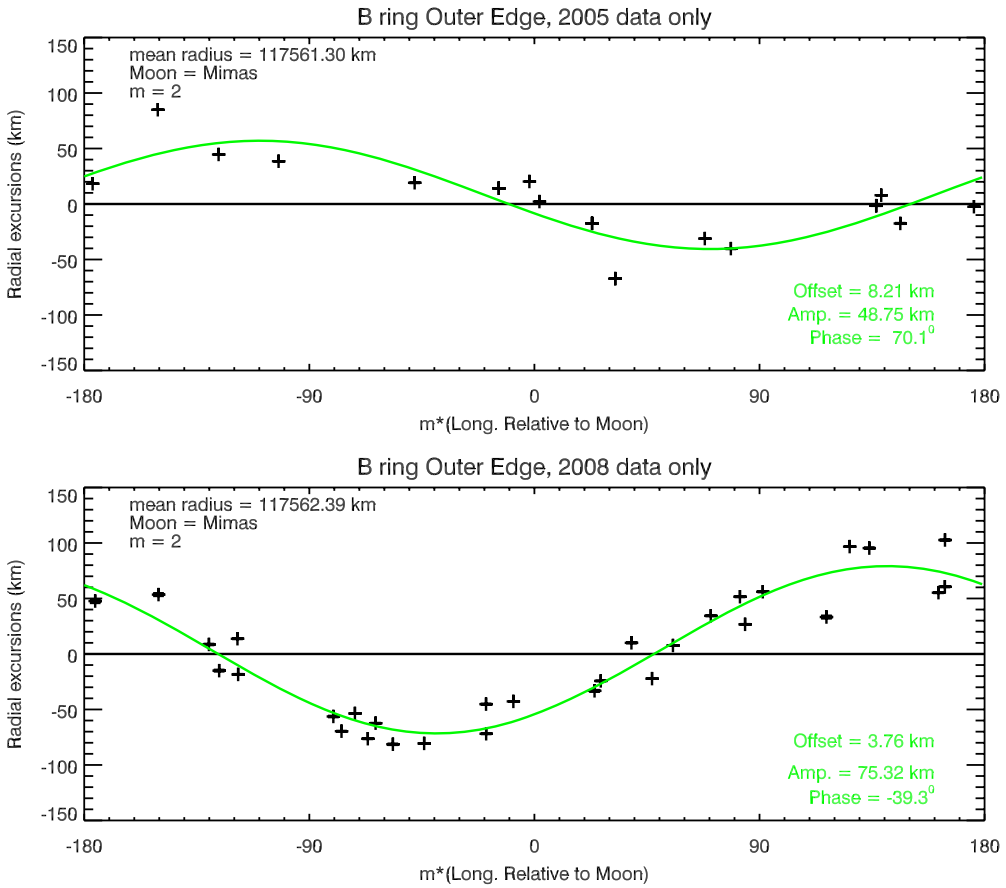

Figure 9. Radial excursions of the B-ring edge measured by the VIMS and RSS experiments in 2005 (top) and by VIMS in 2008 (bottom). In both cases, the data can be reasonably well fit by simple sine curves.

(A color version of this figure is available in the online journal.)

pattern speed is very similar to the expected apsidal precession rate of $5\overset{\circ}{.}061\ \mathrm{day}^{-1}$ for a Keplerian orbit at this radius. For the 2005 data, the best-fit solution has a slightly larger amplitude of about 23 km and the best-fit pattern speed of $4\overset{\circ}{.}19\ \mathrm{day}^{-1}$, 17% slower than the predicted value of $\dot{\varpi}$. However, given the short time-baseline covered by the 2005 data and the limited number of data points available, a pattern speed of $5\overset{\circ}{.}08\ \mathrm{day}^{-1}$ (consistent with the 2008 observations) can also organize the 2005 data reasonably well (see the bottom panel of Figure 10). An attempt to fit a single, coherent $m = 1$ perturbation to both data sets yields multiple equal-quality fits at an array of pattern speeds separated by $360^\circ/3$ years $\simeq 0\overset{\circ}{.}3\ \mathrm{day}^{-1}$. The available data are therefore too sparse to permit us to derive a more precise model of this perturbation or an accurate measurement of the pattern speed. However, the existence of similar $m = 1$ patterns in both the 2005 and 2008 data sets strongly suggests that this is a "permanent" feature of the B-ring edge.

The radial variations in the location of the B-ring edge therefore have at least two components: an $m = 2$ perturbation forced by the strong Mimas 2:1 ILR, with an average radial amplitude of ∼60 km and an orientation which librates (or circulates) with respect to the direction to Mimas, and an $m = 1$ Keplerian ellipse with an amplitude of ∼20 km which freely precesses under the influence of Saturn's oblate figure at roughly $5^\circ\ \mathrm{day}^{-1}$. Even this rather complicated model provides a relatively poor fit, in comparison with those for the eccentric edges in the Cassini Division, with rms residuals of 10–20 km. We suspect that this is due to deficiencies in our model of the $m = 2$ perturbation, whose libration is still not accurately modeled (e.g., we have not yet implemented a model for the amplitude variations), but it is also possible that additional perturbations are present. Efforts to derive more detailed and accurate models of the B-ring edge are underway and will be presented in future work, but already the preliminary results presented here hint at a close connection between the B-ring edge and the Cassini-Division Gaps.

4. THEORETICAL EXPECTATIONS FOR THE B-RING OUTER EDGE

Before delving into the possible connections between the B-ring edge and the Cassini-Division Gaps, it is useful to first take a closer look at the complex behavior of the B-ring's outer edge. In particular, the above data allow several different solutions for the motion of the $m = 2$ component on this edge, all of which have the $m = 2$ pattern drift or move relative to Mimas. We would like to establish whether any of these solutions are plausible in terms of the local dynamical environment. Since a detailed model along the lines of those developed in Borderies et al. (1982) and Hahn et al. (2009) is beyond the scope of this paper, we will instead examine the behavior of isolated ring particle orbits in the vicinity of the Mimas 2:1 ILR. While not conclusive, these simpler calculations do at least demonstrate that the observed variations in the amplitude and orientation of the $m = 2$ pattern are not wildly inconsistent with theoretical expectations.

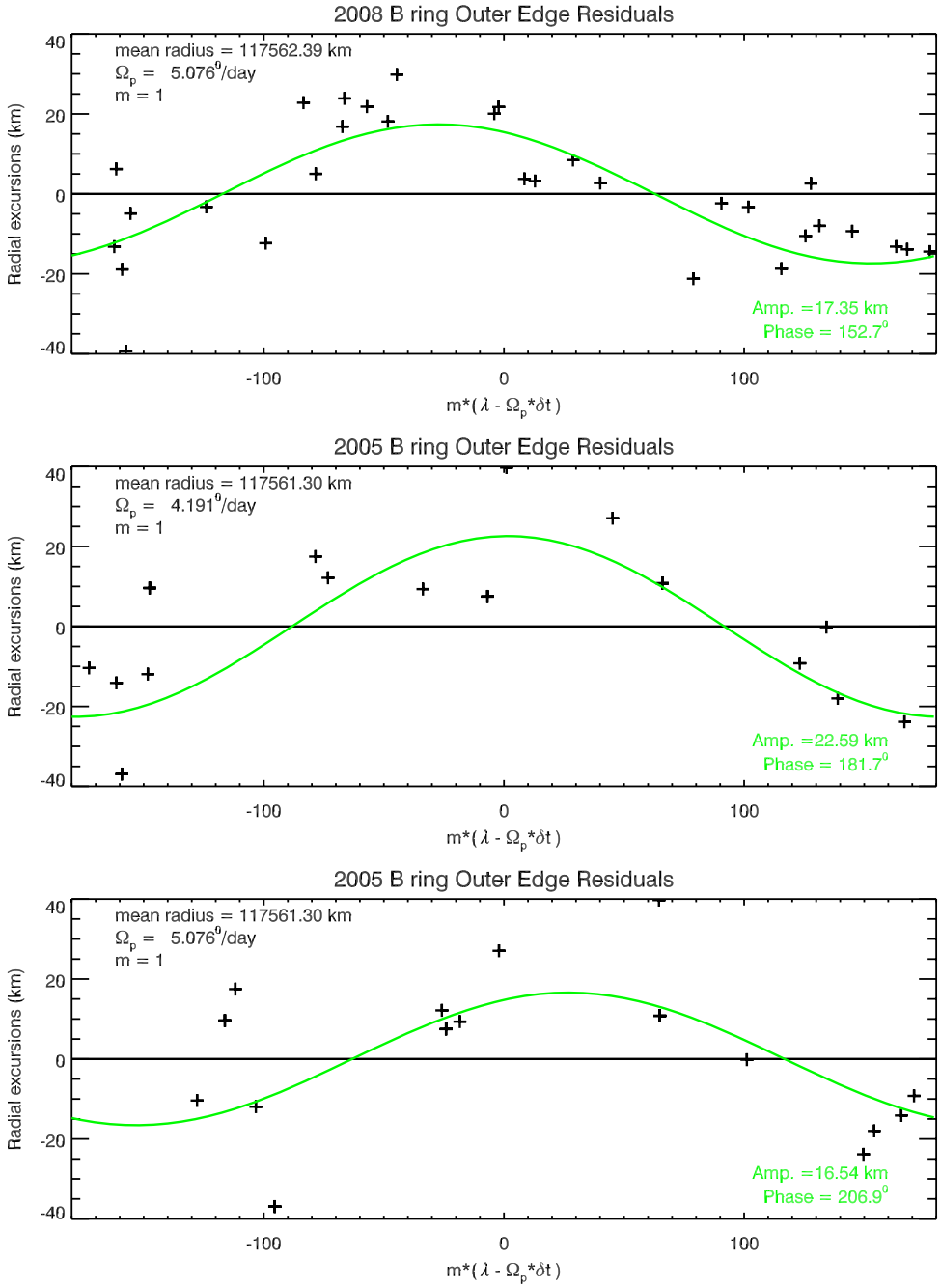

Figure 10. Residual radial variations of the outer edge of the B ring, after removing the $m = 2$ mode pattern associated with the Mimas 2:1 resonance. The top and middle panels show the 2008 and 2005 residuals, respectively, each organized using the best-fit pattern speed. Note the pattern speed for the 2008 data is close to the apsidal precession rate at this location, while the 2005 data is best fit by a 20% slower pattern speed. The bottom panel shows the 2005 data plotted using the same pattern speed as the 2008 data, to illustrate that the data are relatively well organized in this case as well. As before, all times are measured relative to an epoch of 2005-195T02:12:13.557 or a Cassini spacecraft clock time of 150000000.

(A color version of this figure is available in the online journal.)

The following discussion is based on that in Chapter 8 of Murray & Dermott (1999), but couched in terms of the physical coordinates, r and λ, and the standard orbital elements, a, e, and ϖ, rather than a Hamiltonian formalism.

At a first-order ILR, the resonant argument is given by

$$\varphi_{\rm ILR} = (m-1)\lambda + \varpi - m\lambda_s, \tag{11}$$

where m is a positive integer, λ and λ_s refer to the mean longitudes of the test particle and satellite, respectively, and ϖ is the longitude of pericenter of the test particle's orbit. At the so-called exact resonance,

$$\frac{d\varphi_{\rm ILR}}{dt} = (m-1)n + \dot{\varpi}_{\rm sec} - mn_s = 0, \tag{12}$$

where n is the orbital mean motion and $\dot{\varpi}_{\rm sec}$ is the apsidal precession rate of the test particle due to non-resonant perturbations (chiefly the planet's oblateness). For a 2:1 ILR, $m = 2$ and $n_{\rm res} = 2n_s - \dot{\varpi}_{\rm sec}$.

An ensemble of test particles which share common values of semimajor axis a, eccentricity e, and $\varphi_{\rm ILR}$, but different instantaneous values of λ and ϖ, will define a streamline given

by

$$r(\lambda, t) \approx a\,[1 - e\cos(\lambda - \varpi)]\,, \tag{13}$$

or in terms of $\varphi_{\rm ILR}$

$$r(\lambda, t) \approx a\,[1 - e\cos\left(m(\lambda - \lambda_s) - \varphi_{\rm ILR}\right)]\,. \tag{14}$$

This is the same as Equation (6) above, with $A = ae$, $r_0' = a$, and

$$\varphi_{\rm ILR} = 2\phi_L \sin(Lt - \theta_L). \tag{15}$$

Following Murray & Dermott (1999, see their Equation (8.26) and Table 8.5), the corresponding time-averaged disturbing function of the satellite (to lowest order in eccentricity and for zero inclination) is given by

$$\mathcal{R}_{\rm ILR} = \frac{Gm_s}{a_s} f(\alpha) e \cos\varphi_{\rm ILR}, \tag{16}$$

where m_s is the mass of the satellite, $\alpha = a/a_s$, and for $m = 2$ the function $f(\alpha) = -0.75/\alpha$ comes from evaluating the disturbing function. The Lagrange equations which describe the resulting perturbations in the test particle's orbital elements are

$$\frac{dn}{dt} = -3(m-1)\beta n^2 e \sin\varphi_{\rm ILR}, \tag{17}$$

$$\frac{de}{dt} = -\beta n \sin\varphi_{\rm ILR}, \tag{18}$$

$$\frac{d\varpi}{dt} = -\beta n e^{-1}\cos\varphi_{\rm ILR} + \dot{\varpi}_{\rm sec}, \tag{19}$$

$$\frac{d\epsilon}{dt} = -\frac{1}{2}\beta n e \cos\varphi_{\rm ILR}, \tag{20}$$

where we have introduced the dimensionless resonance strength $\beta = -(m_s/M_S)\alpha f(\alpha)$, with M_S the mass of the planet. The quantity ϵ is the longitude at epoch, defined by the usual expression $\lambda = \epsilon + nt$. These are equivalent to Equations (8.28)–(8.31) of Murray & Dermott (1999), except that our definition of the resonant argument in Equation (11) is opposite in sign to theirs. Combining Equations (17), (19), and (20), we can derive an expression for the rate of change of $\varphi_{\rm ILR}$:

$$\frac{d\varphi_{\rm ILR}}{dt} = (m-1)n - mn_s + \dot{\varpi}_{\rm sec} - \left[\frac{\beta n}{e} + \frac{(m-1)\beta n e}{2}\right]\cos\varphi_{\rm ILR}. \tag{21}$$

For small values of e, we can safely neglect the last term in brackets (which arises from Equation (20)).

From Equations (17) and (18), we see that n and e must vary in phase, with

$$\frac{dn}{de} = 3(m-1)ne, \tag{22}$$

so that we may write, to the lowest order in e,

$$n \approx n_0 + \frac{3}{2}(m-1)n_0 e^2, \tag{23}$$

where n_0 is a constant. Substituting this expression for n into Equation (21), and introducing the constant parameter $\nu = (m-1)n_0 - mn_s + \dot{\varpi}_{\rm sec}$, we have our final equation for the resonant variable, correct to the lowest order in e:

$$\frac{d\varphi_{\rm ILR}}{dt} = \nu + \frac{3}{2}(m-1)^2 n_0 e^2 - \frac{\beta n_0}{e}\cos\varphi_{\rm ILR}. \tag{24}$$

The frequency parameter ν is best thought of as a measure of the distance from exact resonance,

$$\nu \approx -\frac{3}{2}(m-1)n_{\rm res}\left(\frac{a - a_{\rm res}}{a_{\rm res}}\right), \tag{25}$$

where $a_{\rm res}$ and $n_{\rm res}$ are the semimajor axis and unperturbed mean motion at exact resonance, defined by Equation (12). Note that $\nu > 0$ for orbits *interior* to $a_{\rm res}$.

Equilibrium solutions to Equations (18) and (24) occur where $e = e_0$ and $\varphi_{\rm ILR} = \varphi_0$, where e_0 and φ_0 are constants in time. Such solutions only exist for $\varphi_0 = 0$ or $\varphi_0 = \pi$, and where the eccentricity satisfies the cubic equation:

$$\nu = \frac{\beta n_0}{e_0}\cos\varphi_0 - \frac{3}{2}(m-1)^2 n_0 e_0^2. \tag{26}$$

For positive values of ν (i.e., interior to $a_{\rm res}$) only a single solution exists, with $\varphi_0 = 0$. But for negative values of ν(i.e., exterior to $a_{\rm res}$) up to three branches of solutions exist, labeled A, B, and C by Murray & Dermott (1999, see their Figure 8.9). Solution A, with $\varphi_0 = 0$, is an extension of the equilibrium solution for $\nu > 0$. Solutions B and C have $\varphi_0 = \pi$, with $e_B \leqslant e_C \leqslant e_A$. Solution C is an unstable equilibrium, and thus of little physical interest, but solutions A and B are both stable. Branches B and C merge at a bifurcation point, where $d\nu/de_0 = 0$,

$$\nu_c = -\frac{3}{2}n_0[3(m-1)^2\beta^2]^{1/3}, \tag{27}$$

and

$$e_c = \left[\frac{\beta}{3(m-1)^2}\right]^{1/3}, \tag{28}$$

and cease to exist for larger values of ν.

For $e \ll e_c$, the equilibrium, or *forced* eccentricity is given approximately by

$$e_0 \approx \beta\frac{n_0}{\nu}\cos\varphi_0, \tag{29}$$

with $\varphi_0 = 0$ for $\nu > 0$ (solution A) and $\varphi_0 = \pi$ for $\nu < 0$ (solution B). For $e \gg e_c$, $\varphi_0 = 0$ (solution A) or π (solution C) and

$$e_0 \approx \left[\frac{2|\nu|}{3n_0(m-1)^2}\right]^{1/2}. \tag{30}$$

At $\nu = 0$, $e_0 = 2^{1/3}e_c$.

In the context of planetary rings, it is usually assumed that we are in the "small-e" regime, with $e \ll e_c$ and a resonantly forced eccentricity and phase given by Equation (29) (see Murray & Dermott 1999, Equation (10.21) and Figure 10.9).

If we now substitute suitable numerical values for the Mimas 2:1 ILR, we find that $a_{\rm res} = 117{,}553.65$ km, $\dot{\varpi}_{\rm sec} = 5.^\circ0613$ day^{-1}, $n_{\rm res} = 2n_s - \dot{\varpi}_{\rm sec} = 758.^\circ9277$ day^{-1}, $\alpha \approx 0.6336$, $m_s/M = 6.60 \times 10^{-8}$ (Jacobson et al. 2006), and $\beta = 4.95\times10^{-8}$. The corresponding eccentricity and frequency at the bifurcation point are $e_c = 0.00255$ and $\nu_c = -0.^\circ0221$ day^{-1}. From Equation (25) we have that

$$\nu \approx -0.^\circ0097/{\rm day}\left(\frac{a - a_{\rm res}}{1\ {\rm km}}\right), \tag{31}$$

so that the bifurcation point occurs at $a - a_{\rm res} = +2.3$ km with a forced amplitude, $ae_c = 299$ km.

Since the maximum radial amplitude observed at the edge of the B ring, $A \simeq 75$ km, or one-quarter of the critical value, we may conclude that the streamlines are indeed in the "small-e" regime. We can then use Equation (29) to estimate the effective value of ν for streamlines at the edge of the B ring. If we adopt an average forced eccentricity of $(0.50 \pm 0.12) \times 10^{-3}$ (i.e., $A = 60 \pm 15$ km), and note that φ appears to librate around 0 rather than π, then we find

$$\nu_{\rm eff} \approx \frac{\beta n_0}{e_0} \cos\varphi_0 = +0.075 \pm 0.^{\circ}019 \text{ day}^{-1} \quad (32)$$

with an effective distance from exact resonance of $a - a_{\rm res} = -8 \pm 2$ km. This may be compared with the observed mean location of the edge of 117,565.4 km, or $a - a_{\rm res} = +12$ km. The B-ring edge thus *behaves* as if it were located 5–10 km interior to the 2:1 resonance, whereas it is *actually* located ~12 km exterior to the resonance. A similar conclusion was reached by Porco et al. (1984) in their study of this edge using *Voyager* observations, though their value of $a - a_{\rm res}$ was less accurate due to uncertainties at that time in the absolute radius scale of the rings.

However, the classical "resonance width" $w_{\rm res}$—the range in semimajor axis over which test particle orbits on opposite sides of exact resonance will overlap due to their 180° difference in φ_0—is given by substituting Equation (25) into Equation (29) and solving for $ae_o = a - a_{\rm res} = w_{\rm res}/2$ (see Murray & Dermott 1999, Equation (10.23)):

$$w_{\rm res} \approx 2a_{\rm res}\left[\frac{2\beta}{3(m-1)}\right]^{1/2} = 43 \text{ km}. \quad (33)$$

(Note that this is actually 1/2 of Murray and Dermott's expression, which includes the radial excursions due to the forced eccentricities.) Within ~20 km of exact resonance, therefore, we cannot expect the above test particle model to give realistic estimates of e_0 as a function of a. In an actual planetary ring, the situation will be further complicated by gravitational and collisional interactions between the ring particles, which will act to prevent the streamline crossing predicted by our simple test-particle model within $\pm w_{\rm res}/2$ of $a_{\rm res}$. Such a model has recently been developed for application to the A- and B-ring edges by Hahn et al. (2009), based on earlier work by Borderies et al. (1982).

Although dissipative collisions within a real ring might be expected to rapidly damp any motion relative to the equilibrium solutions discussed above, our observations of the B-ring edge strongly suggest either that the resonance angle $\varphi_{\rm ILR}$ is librating about an equilibrium value close to 0, or that it is circulating in a retrograde direction (i.e., $\langle d\varphi_{\rm ILR}/dt\rangle < 0$). The equations of motion, Equations (17)–(20), admit of both finite-amplitude oscillations in $\varphi_{\rm ILR}$ and of circulating solutions. For a series of phase portraits of such librations, the interested reader is referred to Figure 8.10 in Murray & Dermott (1999). (Their dimensionless parameter δ is equal to $3\nu/\nu_c$, while their amplitude parameter $\Phi = \frac{1}{2}(e/e_c)^2$.)

In the small-e limit (i.e., $e \ll e_c$), Equation (24) reduces to

$$\frac{d\varphi_{\rm ILR}}{dt} \approx \nu - \frac{\beta n_0}{e}\cos\varphi_{\rm ILR}, \quad (34)$$

while the variation in e is given by Equation (18), where we may set $n \approx n_0$. In this limit, the variations in $\varphi_{\rm ILR}$ are dominated by the resonant effects on ϖ. These coupled equations are most readily solved by introducing the conjugate variables

$$h = e\cos\varphi_{\rm ILR}, \quad k = e\sin\varphi_{\rm ILR}, \quad (35)$$

in terms of which Equations (18) and (34) become

$$\frac{dh}{dt} = -\nu k, \quad (36)$$

$$\frac{dk}{dt} = \nu h - \beta n_0. \quad (37)$$

The solution follows trivially:

$$h(t) = \frac{\beta n_0}{\nu} + e_f\cos(\nu t - \theta), \quad (38)$$

$$k(t) = e_f\sin(\nu t - \theta). \quad (39)$$

Recall that $\beta n/|\nu|$ is the forced eccentricity, e_0, from Equation (29) above. The *free eccentricity*, e_f, and phase angle, θ, are arbitrary constants of the motion, set by the initial conditions. In the h, k plane, the motion is in a circle of radius e_f about the fixed point, $(\pm e_0, 0)$. Interior to the resonance ($\nu > 0$, equilibrium branch A) the motion is counterclockwise about $(+e_0, 0)$, while exterior to the resonance ($\nu < 0$, branch B) the motion is clockwise about $(-e_0, 0)$. In both cases, the angular frequency is simply equal to ν, given by Equation (25) above.

If $e_f < e_0$, the solution describes a librational motion of φ about either 0 (for $\nu > 0$) or π (for $\nu < 0$). The maximum libration amplitude is given by $\varphi_{\rm max} = \sin^{-1}(e_f/e_0)$, while the instantaneous eccentricity is equal to

$$e(t) = \sqrt{h^2 + k^2} = \left[e_0^2 + e_f^2 + 2e_o e_f\cos(\nu t - \theta)\right]^{1/2}. \quad (40)$$

For $e_f > e_0$, the angle $\varphi_{\rm ILR}$ circulates continuously through 2π radians, while e oscillates between $e_f - e_0$ and $e_f + e_0$. Example trajectories for both cases are shown in Figure 8.11 of Murray & Dermott (1999).

Although the form of the small-e librations motivated our choice of the model used to fit the B-ring edge above, we note that even this simple test-particle model implies (1) that the amplitude of the edge, $A = ae$ should oscillate as the edge librates or circulates, and (2) that the variation in the resonant angle, $\varphi_{\rm ILR}$, will not be sinusoidal or linear, unless $e_f \ll e_0$ or $e_0 \gg e_f$. The substantial variations observed in A and $\varphi_{\rm ILR}$ over the course of the Cassini mission to date suggest that the latter is unlikely to be true. A more sophisticated model might therefore be based on the small-e solution above.

Despite these limitations, we note that the best-fitting libration frequencies of $0.^{\circ}058$ and $0.^{\circ}117$ day^{-1} found above are generally consistent with our theoretical estimate of $\nu = 0.075 \pm 0.^{\circ}019$ day^{-1} in Equation (32), based on equating the observed amplitude to the forced eccentricity.

If, on the other hand, the B-ring edge is circulating, then the best-fitting drift rate of $\phi_L L = -0.^{\circ}05$ day^{-1} (compared to Figure 8) implies that $d\varphi_{\rm ILR}/dt = 2\phi_L L \approx -0.^{\circ}10$ day^{-1}, from Equation (15), or $a - a_{\rm res} = +10$ km, which agrees fairly well with the observed mean radius of the edge. Thus, both librating and circulating small-e models seem to be quantitatively consistent with our observations of the B-ring edge, despite their obvious limitations noted above.

For completeness, we did examine the large-e case, but these calculations indicate that a large-e libration is less compatible with the observed motion of the B-ring edge. Not only does the

predicted forced amplitude, $A = ae_0$, exceed 750 km only 5 km outside the resonant radius—10 times the maximum observed value—but the libration frequency is quite slow, reaching only $0\overset{\circ}{.}024$ day^{-1} at $a - a_{\rm res} = 5$ km and $0\overset{\circ}{.}033$ day^{-1} at 20 km. Such low libration frequencies are strongly disfavored by the available data.

5. A POSSIBLE EXPLANATION FOR THE LOCATION OF THE CASSINI-DIVISION GAPS

The above analysis indicates that the structure of the Cassini Division may be more regular than it appears at first glance. Certainly, the Barnard Gap is no longer a mystery, as it seems to be held open by the 5:4 mean motion resonance with Prometheus. Furthermore, the remaining gaps seem to form a pattern. The Herschel, Russell, Jeffreys, Kuiper, Laplace, and Bessel Gaps all seem to have an eccentric inner edge and most of these also have a circular outer edge. (The Huygens, Herschel and Laplace Gaps do not have perfectly circular outer edges, but these are also the gaps which contain dense ringlets, which may complicate the situation.) Furthermore, the six eccentric gap edges seem to define a series of evenly spaced pattern speeds with a characteristic spacing of about $0\overset{\circ}{.}06$ day^{-1}. Even the Huygens Ringlet and the $m = 1$ component of the B-ring edge seem to fall in this sequence. Finally, there is the suggestive coincidence that the $m = 2$ pattern on the B-ring edge could be librating with an angular frequency not too dissimilar from $0\overset{\circ}{.}06$ day^{-1} (although we must caution that other solutions are possible).

Based on these findings, we have developed a novel explanation for the location of the gaps in the Cassini Division. Just as the inner edges of the Huygens and Barnard Gaps are established by resonances with Saturnian satellites (Mimas 2:1 and Prometheus 5:4, respectively), the inner edges of the other gaps are maintained by resonances which involve the edge of the B ring. In the following sections, we demonstrate that the gravitational perturbations from the radial excursions of the B-ring edge, together with perturbations from Mimas, can give rise to terms in the equations of motion that would support the formation of eccentric edges at their observed locations in the Cassini Division.

Note that for the purposes of this theoretical study, we will assume that the orientation of the $m = 2$ pattern on the B-ring edge librates with a frequency of $\sim 0\overset{\circ}{.}06$ day^{-1}, which matches the typical spacing between the pattern speeds of eccentric features in the Cassini Division. This particular solution is clearly the one where the B-ring-edge patterns would be most likely to generate a series of structures like the Cassini-Division Gaps. Thus, an analysis of this case will establish whether such a model has any hope of working. Of course, our current understanding of the data admits the possibility of different libration frequencies or even circulation of the $m = 2$ pattern. If one of these alternate solutions turns out to be correct, then the connection between the B-ring edge and the Cassini Division may still exist but be more complicated, and the simpler analysis presented here could still help clarify this relationship.

5.1. Qualitative Frequency Studies

To determine if any interesting resonances in the Cassini Division could be generated by the B-ring edge, one must write down the gravitational potential associated with the observed structure of the B-ring edge, compute the appropriate terms in the disturbing function, and determine if they could drive structures like those seen in the various gap edges. In this case, however, the data described above already provide hints of what terms in the disturbing function could be involved in generating the observed edges. Therefore, prior to exploring the dynamical environment of the Cassini Division in detail, we will first take a more qualitative look at the situation in order to clarify which terms in the gravitational potentials are likely to be relevant.

The $m = 1$ patterns on the relevant Cassini-Division edges move at speeds close to the expected local apsidal precession rates given Saturn's oblateness (see Table 4). Thus, each edge can be thought of as a collection of particles on freely precessing eccentric orbits whose pericenters are all aligned to produce a coherent structure. Assuming the orientation of the $m = 2$ pattern in the B-ring edge librates at $\sim 0\overset{\circ}{.}06$ day^{-1}, this alignment in pericenters would appear to occur at places where the apsidal precession rate $\dot{\varpi}$ has the following values:

$$\dot{\varpi} = \dot{\varpi}_B - jL, \tag{41}$$

where $\dot{\varpi}_B$ is the apsidal precession rate of the B-ring edge (also the pattern speed of the $m = 1$ component on that edge), j is an integer, and L is the libration frequency of the $m = 2$ pattern in the B-ring edge. Since $\dot{\varpi}$ as a function of a is determined primarily by the higher-order components in Saturn's gravitational field, Equation (41) implicitly specifies the locations of a series of regularly spaced resonances. At these locations, the following quantity is approximately constant:

$$\varphi = \varpi - \varpi_B + jLt. \tag{42}$$

We propose that there is a term in the equations of motion that tries to maintain φ near some value φ_o. Such a term will act to align orbital pericenters and produce a coherent structure on each edge that is stable against small perturbations. In order for this to work, the equation of motion of this resonant argument needs to have a term of the form

$$\frac{d^2\varphi}{dt^2} \simeq -f_o^2 \sin(\varphi - \varphi_o). \tag{43}$$

In this particular situation, the above expression can be rewritten as (assuming $\dot{\varpi}_B$ and L are constant)

$$\frac{d^2\varpi}{dt^2} \simeq -f_o^2 \times \sin(\varpi - \varpi_B + jLt - \varphi_o). \tag{44}$$

Provided such a term exists in the equations of motion, then the pericenters of individual particle orbits could become aligned, forming a coherent $m = 1$ pattern that moves around the planet at the local precession rate established by Saturn's oblateness, consistent with the observations.

Lagrange's planetary equations relate time derivatives in orbital elements like ϖ to derivatives of the disturbing function (e.g., $d\varpi/dt \propto d\mathcal{R}/de$). Thus, in order to determine if $\varphi = \varpi - \varpi_B + jLt$ is a proper resonant argument that can produce a coherent structure, we need to find a term or a combination of terms in the disturbing function that are proportional to $\sin(\varpi - \varpi_B + jLt)$.

The question now is whether such terms are likely to appear in the disturbing function generated by the B-ring edge. We can model the B-ring edge as a collection of mass ribbons, each of which has the characteristic shape

$$r = r_o - d_1 \cos(\phi - \varpi_B) - \tilde{d}_2 \cos(2[\phi - \lambda_{\rm Mimas} - \tilde{\phi}_L]), \tag{45}$$

where ϕ is the azimuthal angle. $\tilde{\phi}_L = \phi_L \times \sin(Lt - \theta_L)$ is the time-variable azimuthal offset due to the edge's libration (see Equation (6) above). Note the term $\tilde{d}_2$ may also have a time-variable component ($\tilde{d}_2 = d_2[1 \pm \delta_2^d \cos(Lt - \theta_L)]$) because the amplitude of the $m = 2$ pattern is apt to change over the course of the libration cycle. In fact, as discussed in Section 4 above, the librations in the amplitude and the phase are likely to be coupled in such a way that neither oscillation is purely sinusoidal, but for the purposes of this analysis we will ignore such complications.

Such mass ribbons will produce a relatively complicated potential, but in general we expect terms in the disturbing function to contain second-order terms of the following form

$$\mathcal{R}_{kl} \propto d_1^{|k|} \tilde{d}_2^{|l|} \cos(k(\lambda - \varpi_B) + l[2\lambda - 2\lambda_{\rm Mimas} - 2\tilde{\phi}_L]), \quad (46)$$

where k and l are various integers and λ is the perturbed particle's mean longitude (assuming the particle's orbit is nearly circular). We can quickly see that any term of this form that contains $\tilde{\phi}_L$ will also contain $\lambda_{\rm Mimas}$, so no term of this form will have the form required to produce something like Equation (44). This suggests that the B-ring edge alone will be unable to produce the resonances required to explain the eccentric edges in the Cassini Division.

All is not lost, however, because there is a possibility that the perturbations from the B-ring edge, acting together with perturbations from the nearby and very powerful Mimas 2:1 ILR, can generate the desired terms in the disturbing function through a sort of three-body resonance. In such a situation, the time derivatives of orbital elements can be proportional to the products of disturbing functions, which means we will get products of the $\mathcal{R}_{kl}$ above with the term responsible for the Mimas 2:1 resonance,

$$\mathcal{R}_{\rm Mimas} \propto m_M \cos(\lambda + \varpi - 2\lambda_{\rm Mimas}), \quad (47)$$

where m_M is the mass of Mimas. This yields terms of the following form:

$$\mathcal{R}'_{k,l} \propto m_M d_1^{|k|} \tilde{d}_2^{|l|} \sin((\lambda + \varpi - 2\lambda_{\rm Mimas}) + k(\lambda - \varpi_B) + l[2\lambda - 2\lambda_{\rm Mimas} - 2\tilde{\phi}_L]). \quad (48)$$

When $k = 1$ and $l = -1$, this term has the promising form

$$\mathcal{R}'_{1,-1} \propto m_M d_1 \tilde{d}_2 \sin(\varpi - \varpi_B + 2\tilde{\phi}_L), \quad (49)$$

or, equivalently

$$\mathcal{R}'_{1,-1} \propto m_M d_1 \tilde{d}_2 \sin(\varpi - \varpi_B + 2\phi_L \sin(Lt - \theta_L)). \quad (50)$$

This term is proportional to something like $\sin(A \times t + B \times \sin(C \times t))$. Note in particular that in this case $\phi_L \simeq 50^\circ$ or nearly 1 radian (see Figure 8), so the coefficient B is actually quite large. Figure 11 shows a Fourier transform of a function of the form $\sin(t + \sin(0.01t))$, which illustrates that this sort of function actually has multiple periodic components (the amplitudes of these different components can be evaluated using Bessel functions; see Gray & Mathews 1895). The above term in the disturbing function can therefore be expressed as the following series:

$$\mathcal{R}'_{1,-1} \propto \sum_{\rm j} C_j \sin(\varpi - \varpi_B + jLt - j\theta_L), \quad (51)$$

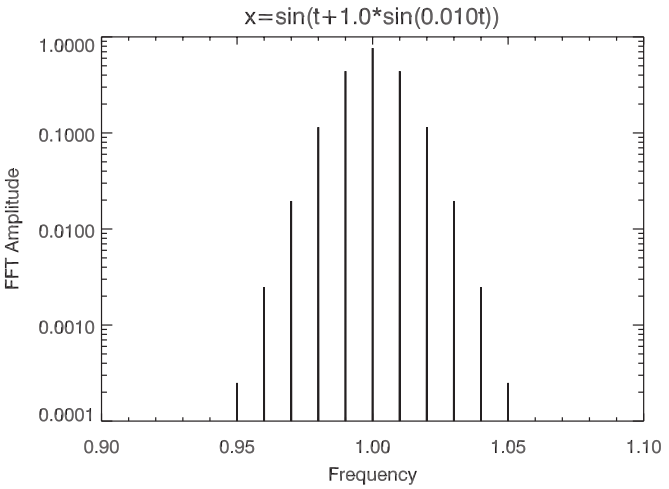

Figure 11. Fourier transform of the function $x = \sin(t + \sin(0.01t))$, showing the multiple frequency components with comparable amplitudes.

which is exactly the form which we are seeking (compared with Equation (44) above). A single disturbing term of the form given in Equation (49) could therefore potentially lead to the formation of multiple, evenly spaced features, like the gaps in the Cassini Division.

Given all this, it seems reasonable to look for three-body-like resonances in the Cassini Division where one of the bodies is Mimas and the other is the B-ring edge. Furthermore, we will be particularly interested in terms in the disturbing function of the B-ring edge that have the form

$$\mathcal{R}_{1,-1} \propto d_1 \tilde{d}_2 \sin([\lambda - \varpi_B] - [2\lambda - 2\lambda_{\rm Mimas} - 2\tilde{\phi}_L]). \quad (52)$$

5.2. Evaluating the Disturbing Function

The above analysis indicates that we will need two pieces of the disturbing function: (1) the part of the disturbing function due to Mimas that goes like $\cos(\lambda + \varpi - 2\lambda_{\rm Mimas})$ and (2) the part of the disturbing function due to the B ring that goes like $\cos(\lambda + \varpi_B - 2\lambda_{\rm Mimas} - 2\tilde{\phi}_L)$.

The relevant part of the Mimas disturbing function is given by Equation (16) above

$$\mathcal{R}_{\rm Mimas} = \frac{G m_M}{a_M} f(a/a_M) e \cos(\lambda + \varpi - 2\lambda_{\rm Mimas}), \quad (53)$$

where m_M and a_M are Mimas' mass and orbital semimajor axis, respectively, while a and e are the particles' semimajor axis and eccentricity (recall that for a 2:1 resonance $f(\alpha) = -0.75/\alpha$).

Of course, extracting the relevant bit of the ring's disturbing function requires more effort. Again, consider a mass ribbon whose position is described by the following equation:

$$r = r_o - \delta r = r_o - d_1 \cos(\phi - \varpi_B) - \tilde{d}_2 \cos(2\phi - \tilde{\phi}_{\rm LM}), \quad (54)$$

where for simplicity of notation we have introduced the term $\tilde{\phi}_{\rm LM} = 2\lambda_{\rm Mimas} + 2\tilde{\phi}_L$.

The disturbing function for a small mass element dm of this ring on a particle at radius r' and longitude λ is given by

$$\mathcal{R}_{dm} = G dm \left[\frac{1}{r'} \sum_{l=1}^{\infty} \left(\frac{r}{r'} \right)^l P_l(\cos\psi) - \frac{r'}{r^2} \cos\psi \right], \quad (55)$$

where ψ is the difference in longitudes between the mass element and the particle of interest, so $\phi = \psi + \lambda$.

The total disturbing function for the ring is then this expression integrated over all ψ

$$\mathcal{R}_{\rm ring} = \frac{Gm_r}{2\pi}\int_o^{2\pi}\left[\frac{1}{r'}\sum_{l=1}^{\infty}\left(\frac{r}{r'}\right)^l P_l(\cos\psi) - \frac{r'}{r^2}\cos\psi\right]d\psi, \tag{56}$$

where m_r is the total mass of the ribbon, which for now is assumed to be uniformly distributed in ϕ.

The terms we are interested in here are proportional to $(\delta r)^2 = (r - r_o)^2$ because

$$(\delta r)^2 = 2d_1\tilde{d}_2\cos(\psi+\lambda-\varpi_B)\cos(2\psi+2\lambda-\tilde{\phi}_{\rm LM})+\cdots, \tag{57}$$

$$(\delta r)^2 = d_1\tilde{d}_2\cos(\psi+\lambda+\varpi_B-\tilde{\phi}_{\rm LM})+\cdots, \tag{58}$$

$$(\delta r)^2 = d_1\tilde{d}_2\cos(\lambda+\varpi_B-\tilde{\phi}_{\rm LM})\cos\psi+\cdots. \tag{59}$$

So this is the lowest order term in $d_1, \tilde{d}_2$ that contains the desired frequency term.

Re-writing $\mathcal{R}_{\rm ring}$ so that δr is explicit, we find

$$\mathcal{R}_{\rm ring} = \frac{Gm_r}{2\pi r'}\int_o^{2\pi}\sum_{l=1}^{\infty}\left(\frac{r_o-\delta r}{r'}\right)^l P_l(\cos\psi)d\psi - \frac{Gm_r r'}{2\pi}\int_o^{2\pi}\frac{1}{(r_o-\delta r)^2}\cos\psi\, d\psi. \tag{60}$$

Expanding both terms and keeping only terms proportional to $(\delta r)^2$, we obtain

$$\mathcal{R}'_{\rm ring} = \frac{Gm_r}{2\pi r' r_o^2}\sum_{l=2}^{\infty}\frac{l(l-1)}{2}\left(\frac{r_o}{r'}\right)^l\left[\int_o^{2\pi}(\delta r)^2 P_l(\cos\psi)d\psi\right] - \frac{3Gm_r r'}{2\pi r_o^4}\int_o^{2\pi}(\delta r)^2\cos\psi\, d\psi. \tag{61}$$

While both parts of this function are non-zero, the second part is a single term while (as we will see below) the first part is a slowly converging series. Thus, at this point we will drop the second term and only keep the parts of the first term containing the element explicitly listed in Equation (59):

$$\mathcal{R}'_{\rm ring} \simeq \frac{Gm_r d_1\tilde{d}_2}{2\pi r' r_o^2}\cos(\lambda+\varpi_B-\tilde{\phi}_{\rm LM})\sum_{l=2}^{\infty}\frac{l}{2}\left(\frac{r_o}{r'}\right)^l \times\left[\int_o^{2\pi}(l-1)\cos\psi\, P_l(\cos\psi)d\psi\right]. \tag{62}$$

It turns out that for large values of l the term in the square brackets becomes 4 for odd l and 0 for even l (see Figure 12). Since $r_o/r' \simeq 1$ in the Cassini Division, the series slowly converges, so we can actually approximate this term as 2. In this approximation

$$\mathcal{R}'_{\rm ring} \simeq \frac{Gm_r d_1\tilde{d}_2}{2\pi r' r_o^2}\cos(\lambda+\varpi_B-\tilde{\phi}_{\rm LM})\sum_{l=2}^{\infty} l\left(\frac{r_o}{r'}\right)^l, \tag{63}$$

and since $\sum l x^l = 1/(1-x)^2$

$$\mathcal{R}'_{\rm ring} \simeq \frac{Gm_r}{2\pi r'}\frac{r'^2}{r_o^2}\frac{d_1\tilde{d}_2}{(r'-r_o)^2}\cos(\lambda+\varpi_B-\tilde{\phi}_{\rm LM}). \tag{64}$$

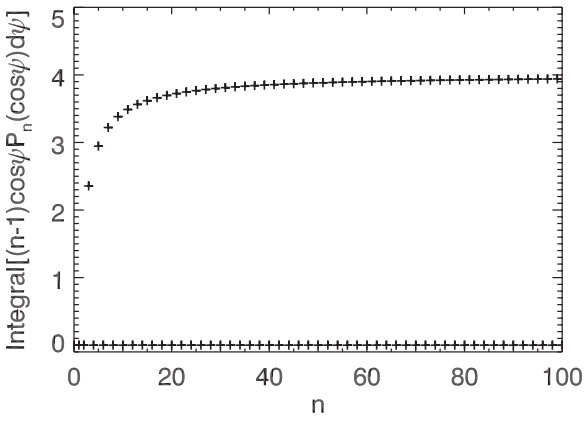

Figure 12. Term $\int_o^{2\pi}(n-1)\cos\psi\, P_n(\cos\psi)d\psi$, evaluated for different values of n. The bottom branch corresponds to even n, where the integral is zero by symmetry. The top branch corresponds to odd n, which asymptotically approaches 4.

Finally, we assume in this case that the particle is on a nearly circular orbit, so $r' \simeq a$, so the final expression for this function is

$$\mathcal{R}^r_{\rm ring} \simeq \frac{Gm_r}{2\pi a}\frac{a^2}{r_o^2}\frac{d_1\tilde{d}_2}{(a-r_o)^2}\cos(\lambda+\varpi_B-\tilde{\phi}_{\rm LM}), \tag{65}$$

where the superscript r indicates that this perturbation is due to the *radial* distortions in the B-ring edge.

This expression gives the disturbing function for a single ribbon of mass total m_r. This perturbation from the entire outer part of the B ring can be approximated as a series of such ribbons with different values of m_r, r_o, d_1, and $\tilde{d}_2$. Since the structure of the B ring is still uncertain at this point (Hahn et al. 2009), for simplicity we will here assume that d_1 and $\tilde{d}_2$ decrease linearly with radius toward the planet:

$$d_1 = D_1\frac{r_o - R_i}{R_o - R_i}, \tag{66}$$

$$\tilde{d}_2 = \tilde{D}_2\frac{r_o - R_i}{R_o - R_i}, \tag{67}$$

where R_o is the mean radius of the B-ring edge, D_1 and $\tilde{D}_2$ are the values of d_1 and $\tilde{d}_2$ at the edge, and $R_i = R_o - W$ is the assumed radius where the amplitudes of the radial excursions in the mass ribbons go to zero. Furthermore, let us assume that the mass of each ribbon is

$$m_r = 2\pi\sigma r_o dr_o, \tag{68}$$

where σ is the (unperturbed) surface mass density of the outer B ring.

If we insert the above expressions for m_r, d_1, and $\tilde{d}_2$ and integrate over all values of r_o between R_i and R_o, assuming that $W = R_o - R_i$ is much less than R_o and $a - R_o$, we find the disturbing function from the entire B ring is given by

$$\mathcal{R}^r_{\rm Ring} \simeq \frac{G\sigma W}{3}\frac{a}{R_o}\frac{D_1\tilde{D}_2}{(a-R_o)^2}\cos(\lambda+\varpi_B-\tilde{\phi}_{\rm LM}). \tag{69}$$

At this point, we should note that the above model of the B ring might be too simplistic, in that it assumes the mass ribbons

are of constant mass. It is of course possible that the mass density of the ribbons ρ also varies with longitude

$$\rho = \frac{m_r}{2\pi}[1 + \mu_1 \cos(\phi - \varpi_B) + \mu_2 \cos(2\phi - \tilde{\phi}_{\rm LM})], \quad (70)$$

where μ_1 and μ_2 are fractional mass density variations along the ribbon. If particles do not collide with one another, then the mass variations μ_1 and μ_2 could be derived from the gradients in the radial variations and orbital parameters. However, in practice, the outer part of the B ring is very dense, so collisions are very important. Indeed preliminary investigations show that the local optical depth of the B ring can vary by over a factor of 2. While we expect these density variations to have some connection with the radial positions of the outer edge, at the present moment we will avoid attempting to estimate μ_1 and μ_2. Regardless of the numerical values of these parameters, such mass anomalies would mean that terms of order $\mu_1 \tilde{d}_2$ and $\mu_2 d_1$would also produce terms with the desired frequency. Following the same procedures as described above, one can show the disturbing function for a ring with both radial excursions and mass anomalies is (ignoring the possibility of phase shifts between the mass anomalies and the radial excursions)

$$\mathcal{R}^{rm}_{\rm Ring} \simeq \frac{G\sigma W}{3}\frac{a}{R_o}\left(\frac{D_1\tilde{D}_2}{(a-R_o)^2} - \mu_2\frac{D_1}{a-R_o} - \mu_1\frac{\tilde{D}_2}{a-R_o}\right) \times \cos(\lambda + \varpi_B - \tilde{\phi}_{\rm LM}). \quad (71)$$

5.3. Numerical Values of the Disturbing Function Terms

Having obtained these two terms, it is worth evaluating their coefficients so we can make some quantitative comparisons of their strength.

For $\mathcal{R}_{\rm Mimas}$ this is relatively easy, since

$$\mathcal{R}_{\rm Mimas} = \frac{Gm_M}{a_M} f(a/a_M) e \cos(\lambda + \varpi - 2\lambda_{\rm Mimas}), \quad (72)$$

or, equivalently

$$\mathcal{R}_{\rm Mimas} = \frac{Gm_M}{a^2}\frac{a}{a_M} f(a/a_M)(ae)\cos(\lambda + \varpi - 2\lambda_{\rm Mimas}). \quad (73)$$

Given $m_M \simeq 4 \times 10^{19}$ kg, and $(a/a_M) f(a/a_M) \simeq -0.75$ for a 2:1 resonance, and assuming $a \simeq 118{,}500$ km and $ae \simeq 5$ km (appropriate for the Russell Gap), we find

$$\mathcal{R}_{\rm Mimas} = -7.1 \times 10^{-4} m^2/s^2 \left(\frac{ae}{5\ {\rm km}}\right)\left(\frac{118{,}500\ {\rm km}}{a}\right)^2 \times \cos(\lambda + \varpi - 2\lambda_{\rm Mimas}). \quad (74)$$

For $\mathcal{R}_{\rm Ring}$ there are more uncertain terms. First considering the simpler case of pure radial excursions in the ring (Equation 69):

$$\mathcal{R}^r_{\rm Ring} \simeq \frac{G\sigma W}{3}\frac{a}{R_o}\frac{D_1\tilde{D}_2}{(a-R_o)^2}\cos(\lambda + \varpi_B - \tilde{\phi}_{\rm LM}). \quad (75)$$

Again, assume $a \simeq 118{,}500$ km for reference. Also, based on our measurements, we will assume $R_o \simeq 117{,}500$ km, $D_1 \simeq 20$ km, and $\tilde{D}_2 \simeq 60$ km. For rough purposes, we will use a surface mass density of $\sigma \simeq 100$ g cm^{-2}and $W \simeq 100$ km, though these parameters are less well constrained. Substituting these numbers into the above expression gives the following result:

$$\mathcal{R}^r_{\rm Ring} \simeq 2.7 \times 10^{-6} m^2/s^2 \times \left(\frac{\sigma}{100\ {\rm g\ cm^{-2}}}\right)\left(\frac{W}{100\ {\rm km}}\right) \times \left(\frac{a}{118{,}500\ {\rm km}}\right)\left(\frac{D_1}{20\ {\rm km}}\right)\left(\frac{\tilde{D}_2}{60\ {\rm km}}\right)\left(\frac{1000\ {\rm km}}{(a-R_o)}\right)^2 \times \cos(\lambda + \varpi_B - \tilde{\phi}_{\rm LM}). \quad (76)$$

Thus, the perturbations from the B ring are about 200 times weaker than those from the 2:1 Mimas resonance. While this is a rather large factor, it is not many orders of magnitude. Also note that the perturbations from the ring could be even larger if there are significant variations in the mass of the ribbons with longitude.

5.4. The Pseudo-Three-Body Resonance

To complete the argument that the perturbations from the B ring and Mimas can act in concert to align the orbit pericenters in the Cassini Division, we will now demonstrate the existence of three-body-like resonances involving these objects. First, recall Equation (44), and realize that the overall goal is to find a term in $d^2\varpi/dt^2$ that is proportional to $\sin(\varpi - \varpi_B + jLt - \varphi_o)$. To do this, we need to express $d^2\varpi/dt^2$ in terms of the disturbing function, which can be done by using the Lagrange planetary equations.

Assuming the particles in the Cassini Division have no inclination, and keeping only terms to lowest order in eccentricity e,

$$\frac{d\varpi}{dt} = \frac{1}{na^2e}\frac{\partial \mathcal{R}}{\partial e} + \dot{\varpi}_{\rm sec}, \quad (77)$$

where $\dot{\varpi}_{\rm sec}$ is again the precession induced by Saturn's oblateness, which we will assume here to be a constant at any given semimajor axis a. This means that

$$\frac{d^2\varpi}{dt^2} = \frac{d}{dt}\left(\frac{1}{na^2e}\frac{\partial \mathcal{R}}{\partial e}\right). \quad (78)$$

In this case, we are only interested in the terms $\mathcal{R}_{\rm Mimas}$ and $\mathcal{R}_{\rm Ring}$ derived above, and $\mathcal{R}_{\rm Ring}$ does not depend on the eccentricity e, so this equation simplifies to

$$\frac{d^2\varpi}{dt^2} = \frac{d}{dt}\left(\frac{1}{na^2e}\frac{\partial \mathcal{R}_{\rm Mimas}}{\partial e}\right). \quad (79)$$

Which can be expanded using Kepler's third law to give

$$\frac{d^2\varpi}{dt^2} = \frac{-1}{na^2e}\left[\frac{1}{e}\frac{\partial \mathcal{R}_{\rm Mimas}}{\partial e}\frac{de}{dt} + \frac{1}{2a}\frac{\partial \mathcal{R}_{\rm Mimas}}{\partial e}\frac{da}{dt} - \frac{d}{dt}\left(\frac{\partial \mathcal{R}_{\rm Mimas}}{\partial e}\right)\right]. \quad (80)$$

Since de/dt and da/dt can be expressed in terms of derivatives of the disturbing function, the first two terms in this expression naturally give a product of two disturbing functions, enabling the term $\mathcal{R}_{\rm Ring}$ to mix with $\mathcal{R}_{\rm Mimas}$ to obtain the desired frequency. However, the third term can also do this since

$$\frac{d}{dt}\left(\frac{\partial \mathcal{R}_{\rm Mimas}}{\partial e}\right) = \frac{\partial^2 \mathcal{R}_{\rm Mimas}}{\partial \epsilon \partial e}\frac{d\epsilon}{dt} + \frac{\partial^2 \mathcal{R}_{\rm Mimas}}{\partial a \partial e}\frac{da}{dt} + \cdots. \quad (81)$$

Note that other derivatives are not of interest here because either they are zero or because they do not lead to terms with the appropriate frequencies. For example, $\partial^2\mathcal{R}_{\rm Mimas}/(\partial e)^2 = 0$, and any term involving $d\varpi/dt$ cannot give a useful term because $\mathcal{R}_{\rm Ring}$ is independent of e. Thus,

$$\frac{d^2\varpi}{dt^2} = \frac{-1}{na^2e}\left[\frac{1}{e}\frac{\partial\mathcal{R}_{\rm Mimas}}{\partial e}\frac{de}{dt} + \left(\frac{1}{2a}\frac{\partial\mathcal{R}_{\rm Mimas}}{\partial e} - \frac{\partial^2\mathcal{R}_{\rm Mimas}}{\partial a\partial e}\right)\frac{da}{dt} - \frac{\partial^2\mathcal{R}_{\rm Mimas}}{\partial\epsilon\partial e}\frac{d\epsilon}{dt}\right]. \quad (82)$$

Now we can use the following Lagrange equations:

$$\frac{da}{dt} = \frac{2}{na}\frac{\partial\mathcal{R}}{\partial\epsilon}, \quad (83)$$

$$\frac{de}{dt} = -\frac{e}{2na^2}\frac{\partial\mathcal{R}}{\partial\epsilon} - \frac{1}{na^2e}\frac{\partial\mathcal{R}}{\partial\varpi}, \quad (84)$$

$$\frac{d\epsilon}{dt} = -\frac{2}{na}\frac{\partial\mathcal{R}}{\partial a} + \frac{e}{2na^2}\frac{\partial\mathcal{R}}{\partial e}. \quad (85)$$

Note that we want terms involving a product of $\mathcal{R}_{\rm Mimas}$ and $\mathcal{R}_{\rm Ring}$, so only derivatives of the latter will be of interest here. Furthermore, since $\mathcal{R}_{\rm Ring}$ only depends on $\lambda = nt + \epsilon$ and a, only the first term in each equation will contribute.

Hence, substituting and simplifying

$$\frac{d^2\varpi}{dt^2} = \frac{-1}{n^2a^4e}\left[\left(\frac{1}{2}\frac{\partial\mathcal{R}_{\rm Mimas}}{\partial e} - \frac{a}{2}\frac{\partial^2\mathcal{R}_{\rm Mimas}}{\partial a\partial e}\right)\frac{\partial\mathcal{R}_{\rm Ring}}{\partial\epsilon} + 2a\frac{\partial^2\mathcal{R}_{\rm Mimas}}{\partial\epsilon\partial e}\frac{\partial\mathcal{R}_{\rm Ring}}{\partial a}\right]. \quad (86)$$

Notice that since $\mathcal{R}_{\rm Mimas}$ depends on various powers of a, $\partial^2\mathcal{R}_{\rm Mimas}/\partial a\partial e$ is of order $a^{-1}\partial\mathcal{R}_{\rm Mimas}/\partial e$, so all the elements of the first term are of the same order. However, since $\mathcal{R}_{\rm Ring} \propto (a - R_o)^{-x}$, $\partial\mathcal{R}_{\rm Ring}/\partial a$ has terms that are of order $(a - R_o)^{-1}\mathcal{R}_{\rm Ring}$, and since $a - R_o$ is much less than a, this means the latter term is much larger, so we can approximate

$$\frac{d^2\varpi}{dt^2} \simeq \frac{-2a}{n^2a^4e}\frac{\partial^2\mathcal{R}_{\rm Mimas}}{\partial\epsilon\partial e}\frac{\partial\mathcal{R}_{\rm Ring}}{\partial a}. \quad (87)$$

Substituting Equations (53) and (69) into this expression (i.e., assuming $\mu_1 = \mu_2 = 0$), we get

$$\frac{d^2\varpi}{dt^2} = \frac{2a}{n^2a^4e}\left[\frac{Gm_M}{a_M}f(a/a_M)\sin(\lambda + \varpi - 2\lambda_{\rm Mimas})\right] \times \left[\frac{2G\sigma W}{3}\frac{a}{R_o}\frac{D_1\tilde{D}_2}{(a - R_o)^3}\cos(\lambda + \varpi_B - \tilde{\phi}_{\rm LM})\right]. \quad (88)$$

Keeping only the desired long-period term, and recalling that $\tilde{\phi}_{\rm LM} = 2\lambda_{\rm Mimas} + 2\tilde{\phi}_L$, this becomes

$$\frac{d^2\varpi}{dt^2} = \frac{2}{3}\frac{n^2}{e}\left[\frac{m_M}{M_S}\frac{a}{a_M}f(a/a_M)\right]\left[\frac{\sigma W R_o}{M_S}\frac{a^2}{R_o^2}\frac{aD_1\tilde{D}_2}{(a - R_o)^3}\right] \times \sin(\varpi - \varpi_B + 2\tilde{\phi}_L). \quad (89)$$

Note that for a 2:1 resonance $a/a_M f(a/a_M) \simeq -0.75$ (see Table 8.5 in Murray & Dermott 1999), so this equation can be written as

$$\frac{d^2\varpi}{dt^2} = -f_o^2\sin(\varpi - \varpi_B + 2\tilde{\phi}_L), \quad (90)$$

where

$$f_o^2 = \frac{2}{3}\frac{n^2}{e}\left[\frac{m_M}{M_S}\frac{a}{a_M}|f(a/a_M)|\right]\left[\frac{\sigma W R_o}{M_S}\frac{a^2}{R_o^2}\frac{aD_1\tilde{D}_2}{(a - R_o)^3}\right] \quad (91)$$

is a positive quantity that indicates the strength of this resonance.

Recall that compound trigonometric functions like $\sin(\varpi - \varpi_B + 2\tilde{\phi}_L) = \sin(\varpi - \varpi_B + 2\phi_L\sin(Lt - \theta_L))$ can be expressed as a series of terms of the form $\sin(\varpi - \varpi_B + jLt)$. We may therefore expand the right-hand side of Equation (90) into the series of terms

$$\frac{d^2\varpi}{dt^2} = \sum_j -f_j^2\sin(\varpi - \varpi_B + jLt), \quad (92)$$

where $f_j^2 = C_j f_o^2$ measures the strength of the individual resonances. As shown in Figure 11, C_j will in general be a decreasing function of j, but for large-amplitude librations C_j would not be much less than unity for most j in the Cassini Division.

If we consider the resonant argument $\varphi_j = \varpi - \varpi_B + jLt$, Equation (92) says that there is a term in the equation of motion:

$$\ddot{\varphi}_j = -f_j^2\sin\varphi_j. \quad (93)$$

Since $\ddot{\varphi}_j = \frac{d}{d\varphi_j}(\dot{\varphi}_j{}^2/2)$, this means

$$\dot{\varphi}_j{}^2 = \dot{\varphi}_o^2 - 4f_j^2\sin^2(\varphi_j/2), \quad (94)$$

where $\dot{\varphi}_o$ is the value of $\dot{\varphi}_j$ where $\varphi_j = 0$. Note that a librating solution to this equation of motion will only exist if $\dot{\varphi}_j = 0$ for some value of φ_j. This will only happen if $\dot{\varphi}_o^2 < 4f_j^2$. Or, in other words, when

$$|\dot{\varpi}_o - \dot{\varpi}_B - jL| < 2f_j, \quad (95)$$

where $\dot{\varpi}_o$ is the apsidal precession rate when $\varphi = 0$. Now, the apsidal precession rate in the Cassini Division is dominated by Saturn's oblateness. Thus, this resonance will only be able to confine the pericenter locations over a region in the rings where the precession rate is within $2f_j$ of $\dot{\varpi}_B - jL$. Inserting the same numbers used in the previous section into Equation (91), we find that in the simple case without mass anomalies (and the amplitude of the $m = 2$ pattern on the B-ring edge is nearly constant)

$$f_j^2 \simeq 7\times10^{-22}/s^2 C_j\left(\frac{5\text{ km}}{ae}\right)\left(\frac{\sigma}{100\text{ g cm}^{-2}}\right)\left(\frac{W}{100\text{ km}}\right) \times \left(\frac{D_1}{20\text{ km}}\right)\left(\frac{\tilde{D}_2}{60\text{ km}}\right)\left(\frac{1000\text{ km}}{a - R_o}\right)^3, \quad (96)$$

so $2f_j$ is of order 5×10^{-11}/s or 0.00025 day^{-1}. Assuming the precession rates are dominated by Saturn's oblateness (so $\delta\dot{\varpi}/\dot{\varpi} \simeq (7/2)\delta a/a$), this range in precession rates corresponds to a range in semimajor axis on the order of a few

kilometers. These resonances should therefore be able to align the pericenters of particle orbits over a region in the rings a few kilometers across, which is comparable to the amplitudes of the observed eccentric features. This result is encouraging, although we must point out that this analysis merely demonstrates that eccentric orbits within a few kilometers of the resonance can have their pericenters aligned by these resonances. This analysis does not determine the actual eccentricity of individual particle orbits near these resonances, which must be the subject of future work.

6. DISCUSSION OF POTENTIAL FURTHER WORK

The above analysis shows that if the orientation of the B-ring edge librates at $\sim 0\overset{\circ}{.}06\ \mathrm{day}^{-1}$, then the combined gravitational perturbations from the B ring and Mimas should align the pericenters of particle orbits at the observed locations of the eccentric gap edges in the Cassini Division. Furthermore, if the physical parameters of the B ring are close to the values assumed above, then particles with aligned orbital pericenters will extend over a range of semimajor axis comparable to the observed amplitudes of the eccentric features in the Cassini Division, which is needed to avoid streamline crossing. Both of these findings lend support to the notion that the gaps in the Cassini Division may indeed be generated by pseudo-three-body resonances involving perturbations from Mimas and the B-ring edge. At the same time, it is also clear that more work needs to be done to develop a complete model of how the Cassini-Division Gaps are formed in this sort of scenario. While such a complete model is beyond the scope of this paper, we will describe in this section what we see as productive avenues for future work toward this goal.

First of all, while the above calculations provide an explanation for why there should be coherent eccentric features at the observed locations of the inner edges of the gaps in the Cassini Division, this analysis does not yet provide a physical explanation of why gaps should form at these locations. We expect that once the gaps have formed, the relevant resonances should maintain the eccentric shape of the inner edges by aligning the pericenters of the relevant particles' orbits. Furthermore, we speculate that the mass anomaly produced by the eccentric inner edge of each gap may help keep the outer edge from diffusing inwards via a modified shepherding mechanism in which the periodic radial and tangential gravitational forces from the eccentric inner edge cause the semimajor axes of the particles on the gap's outer edge to migrate outwards. While Rappaport (1998) determined that the torque from a simple precessing eccentric ringlet is always negative and is therefore unable to confine the outer edge of a gap, the perturbations from eccentric edges (which could involve significant mass anomalies as well as radial excursions) have not yet been thoroughly investigated. Regardless of the specific shepherding mechanism, any successful model of the gap outer edges must be consistent with the observed near-circularity of the outer edges.

While further analytical calculations could clarify which torques might be able to hold open these gaps, numerical studies may be needed to determine how the eccentric inner edges form in the first place. The above calculations suggest that the pericenters of eccentric orbits will become aligned, but they do not indicate whether there is any term in the equations of motion that would tend to generate eccentricities at these locations. While it is possible that such terms are produced by some combination of the various perturbations described above, it is also possible that the eccentricities are generated by an instability in the Cassini Division itself. If particle collisions produce small eccentricities, which are in turn aligned by the above resonance, this will produce small anomalies in the local gravitational field that could then drive larger eccentricities in the region, which will also become aligned, until an eccentric edge is formed. If we can better understand how these edges form, we may be able to convert the observed amplitudes of the radial excursions into constraints on the physical characteristics of the B ring such as its mass density.

Whereas the amplitude of the edges' radial excursions should be related to the physical properties of the B-ring edge, the orientations of the $m = 1$ patterns should be related simply to the kinematics of the B-ring edge. In the idealized model given above, the aligned pericenter locations for the different edges are determined by the movements of the different components in the B-ring edge, and we expect this to be the case in the actual Cassini Division as well. However, the actual pericenter locations of the eccentric Cassini-Division features could be affected by finite mass anomalies in the outer B ring, as well as variations in the amplitude of the $m = 2$ pattern in the B-ring edge. Given that these aspects of the B-ring edge are not yet well modeled, we cannot yet predict the absolute orientation of the Cassini-Division edges at any given time. In fact, if one accepts that the eccentric Cassini-Division edges are produced by the sorts of resonances described above, one could even use the observed amplitudes and orientations of the different eccentric edges to place constraints on the time variability in the B-ring's edge.

More generally, the above model was developed assuming the $m = 2$ pattern in the B-ring edge librates with a frequency of around $0\overset{\circ}{.}06\ \mathrm{day}^{-1}$, which matches the spacing in the observed pattern speeds of the eccentric features in the Cassini Division. More work needs to be done to confirm that this particular solution is indeed the correct one. Beyond considering more data (e.g., from Cassini images, J. N. Spitale & C. C. Porco, 2010, in preparation), more sophisticated theoretical modeling of the B-ring edge may be able to better constrain the likely solutions. Even if one of the other possible solutions for the motion of the $m = 2$ pattern turns out to be correct, a variant of the above model may still be able to produce the observed pattern in the locations of the Cassini-Division features. For example, if the $m = 2$ pattern is actually circulating instead of librating, then its amplitude and drift rate will periodically change as it drifts relative to Mimas, which should produce a series of resonant terms in the equations analogous to those derived above.

Finally, a full understanding of the Cassini-Division Gaps will also need to encompass the non-circular ringlets in the Huygens, Herschel, and Laplace Gaps. The Huygens Ringlet, being the most eccentric feature in the Cassini Division, may turn out to be the limiting case of an eccentric edge. The origin of the Laplace Ringlet may be connected with the second-order Pandora resonance on its inner edge (Colwell et al. 2009). Even so, the Herschel Ringlet remains largely mysterious.

7. CONCLUSIONS

1. The outer edges of five of the eight named gaps in the Cassini Division (that is, all the gaps that do not contain dense ringlets) are circular to within 1 km.
2. The inner edges of six of the eight gaps in the Cassini Division (that is, all of the gap inner edges that do not lie near first-order Lindblad resonances with known satellites) are eccentric, with $m = 1$ radial variations that drift around

the planet at rates close to the expected apsidal precession rates.

3. The radial excursions in the inner edge of the Barnard Gap, which lies close to the 5:4 ILR with Prometheus, do appear to have an $m = 5$ component tied to that moon.
4. The radial excursions in the outer edge of the B ring, which lies close to the 2:1 ILR with Mimas, have an $m = 2$ component. However, the amplitude of the pattern and its orientation relative to Mimas change with time. While the available data do not yet determine a unique solution for the motion of the $m = 2$ pattern, one possibility is that it librates relative to Mimas with a frequency $\sim 0.^{\circ}06$ day^{-1} and an amplitude of $\sim 50^{\circ}$ in longitude or a frequency of 0.12 deg/day and an amplitude of $\sim$30 degrees.
5. In addition to the $m = 2$ pattern, the B-ring edge also appears to have an $m = 1$ component that drifts around the planet at a rate close to the expected apsidal precession rate at the B-ring edge of $5.^{\circ}06$ day^{-1}.
6. The pattern speeds of the eccentric features in the Cassini Division, including the Huygens Ringlet and the $m = 1$ component of the B-ring edge, appear to form a regular series given by $\Omega_p = \dot{\varpi}_B - jL$, where $j = 0, 1, 2, 3, \ldots, 7$, $\dot{\varpi}_B \simeq 5.^{\circ}06$ day^{-1} is the apsidal precession rate at the B-ring edge, and $L \simeq 0.^{\circ}06$ day^{-1} is a likely value for the libration frequency of the $m = 2$ component in the B-ring edge.
7. By combining gravitational perturbations from both components of the B-ring edge with the perturbations from the 2:1 Mimas ILR, one can find terms in the equations of particle motion of the form $\ddot{\varpi} \propto \sin(\varpi - \varpi_B + jLt)$. Such terms could act to align the pericenters of particle orbits at the locations of the eccentric inner edges of each of the gaps, and therefore could explain the locations of the gaps in the Cassini Division.

This work was carried out with financial support from NASA via the Cassini–Huygens program. We acknowledge the support of the Cassini Project and the VIMS team. We thank M. Evans, M. Tiscareno, and R. French for help in the development and validation of the code used to reconstruct the occultation geometries. We also thank the RSS team for sharing their data on the B-ring edge in advance of publication. We also thank J. Burns, J. Cuzzi, C. Murray, N. Rappaport, J. Spitale, and M. Tiscareno for stimulating and useful conversations.

REFERENCES

Borderies, N., Goldreich, P., & Tremaine, S. 1982, Nature, 299, 209
Bosh, A. S., Olkin, C. B., French, R. G., & Nicholson, P. D. 2002, Icarus, 157, 57
Brown, R. H., et al. 2004, Space Sci. Rev., 115, 111
Colwell, J. E., Cooney, J. H., Esposito, L. W., & Sremčević, M. 2009, Icarus, 200, 574
Colwell, J. E., Nicholson, P. D., Tiscareno, M. S., Murray, C. D., French, R. G., & Marouf, E. A. 2009, in Saturn from Cassini-Huygens, ed. M. Dougherty, L. Esposito, & S. M. Krimigis (Berlin: Springer), 13
Elliot, J. L., et al. 1993, AJ, 106, 2544
Esposito, L. W., Harris, C. C., & Simmons, K. E. 1987, ApJS, 63, 749
Esposito, L. W., et al. 1983, J. Geophys. Res., 88, 8643
Flynn, B. C., & Cuzzi, J. N. 1989, Icarus, 82, 180
French, R. G., Kangas, J. A., & Elliot, J. L. 1986, Science, 231, 480
French, R. G., Marouf, E. A., Rappaport, N. J., & McGhee, C. A. 2009, AJ, submitted
French, R. G., Nicholson, P. D., Porco, C. C., & Marouf, E. A. 1991, in Uranus, ed. J. T. Bergstralh, E. D. Miner, & M. S. Matthews (Tucson, AZ: Univ. of Arizona Press), 327
French, R. G., et al. 1993, Icarus, 103, 163
Goldreich, P., & Tremaine, S. D. 1978, Icarus, 34, 240
Gray, G., & Mathews, M. A. 1895, A Treatise on Bessel Functions and their Applications to Physics (Macmillan: London)
Hahn, J. M., Spitale, J. N., & Porco, C. C. 2009, ApJ, 699, 686
Harper, D., & Taylor, D. B. 1993, A&A, 268, 326
Jacobson, R. A., et al. 2006, AJ, 132, 2520
Lane, A. L., et al. 1982, Science, 215, 537
Lissauer, J. J., Shu, F. H., & Cuzzi, J. N. 1981, Nature, 292, 707
Marouf, E. A., & Tyler, G. L. 1986, Nature, 323, 31
Murray, C. D., & Dermott, S. F. 1999, Solar System Dynamics (Cambridge: Cambridge Univ. Press)
Nicholson, P. D., & Hedman, M. H. 2009, Icarus, in press
Nicholson, P. D., & Porco, C. C. 1988, J. Geophys. Res., 93, 10209
Porco, C., Danielson, G. E., Goldreich, P., Holberg, J. B., & Lane, A. L. 1984, Icarus, 60, 17
Rappaport, N. 1998, Icarus, 132, 36
Smith, B. A., et al. 1982, Science, 215, 504
Spitale, J., & Porco, C. C. 2006, BAAS, 38, 670
Spitale, J. N., Porco, C. C., & Colwell, J. 2008, BAAS, 40, 423
Turtle, E., Porco, C., Haemmerle, V., Hubbard, W., & Clark, R. 1991, BAAS, 23, 1179
Tyler, G. L., Marouf, E. A., Simpson, R. A., Zebker, H. A., & Eshleman, V. R. 1983, Icarus, 54, 160